

This is the accepted manuscript made available via CHORUS. The article has been published as:

Emergence of rotational bands in ab initio no-core configuration interaction calculations of the Be isotopes

P. Maris, M. A. Caprio, and J. P. Vary

Phys. Rev. C **91**, 014310 — Published 15 January 2015

DOI: [10.1103/PhysRevC.91.014310](https://doi.org/10.1103/PhysRevC.91.014310)

Emergence of rotational bands in *ab initio* no-core configuration interaction calculations of the Be isotopes

P. Maris,¹ M. A. Caprio,² and J. P. Vary¹

¹*Department of Physics and Astronomy,*

Iowa State University, Ames, Iowa 50011-3160, USA

²*Department of Physics, University of Notre Dame,*

Notre Dame, Indiana 46556-5670, USA

(Dated: November 25, 2014)

The emergence of rotational bands is observed in no-core configuration interaction (NCCI) calculations for the Be isotopes ($7 \leq A \leq 12$), as evidenced by rotational patterns for excitation energies, electromagnetic moments, and electromagnetic transitions. Yrast and low-lying excited bands are found. The results indicate well-developed rotational structure in NCCI calculations, using the JISP16 realistic nucleon-nucleon interaction within finite, computationally-accessible configuration spaces.

I. INTRODUCTION

Nuclei exhibit a wealth of collective phenomena, including clustering, rotation, and pairing [1–3]. Collective dynamics have been extensively modeled in macroscopic phenomenological descriptions [1, 3–5]. Aspects of collectivity may also be obtained microscopically in the conventional shell model, with an inert core and effective valence interactions, *e.g.*, Elliott SU(3) rotation [6, 7] or rotation in large-scale nuclear structure calculations of medium-mass nuclei [8]. However, recent developments in large-scale calculations have brought significant progress in the *ab initio* description of light nuclei (*e.g.*, Refs. [9–14]). We may now therefore hope to observe the emergence of collective phenomena directly from first principles — that is, in a fully *ab initio* calculation of the nucleus, as a many-body system in which all the constituent protons and neutrons participate, with realistic interactions.

In *ab initio* no-core configuration interaction (NCCI) approaches — such as the no-core shell model (NCSM) [14, 15], no-core full configuration (NCFC) [16], importance-truncated

NCSM (IT-NCSM) [17, 18], no-core Monte Carlo shell model (MCSM) [19], and symmetry-adapted NCSM (SA-NCSM) [20, 21] methods — the nuclear many-body bound-state eigenproblem is formulated as a Hamiltonian matrix diagonalization problem. The Hamiltonian is represented with respect to a basis of antisymmetrized products of single-particle states, generally harmonic oscillator states. (For the lightest nuclei, an antisymmetrized basis in Jacobi coordinates has also been used.) The problem is solved for the full system of A nucleons, *i.e.*, with no inert core. In practice, such calculations must be carried out in a finite space, typically obtained by truncating the many-body basis according to a maximum allowed number N_{max} of oscillator excitations above the lowest oscillator configuration (*e.g.*, Ref. [22]). With increasing N_{max} , the results converge towards those which would be achieved in the full, infinite-dimensional space for the many-body system.

Computational restrictions limit the extent to which converged calculations can be obtained for the observables needed to identify collective phenomena. In particular, the observables most indicative of rotational collectivity — $E2$ moments and transition strengths — present special challenges for convergence in an NCCI approach [23, 24], due to their sensitivity to the large-radius asymptotic portions of the nuclear wave function. Nonetheless, signatures of collective phenomena, *e.g.*, deformation and clustering, have already been obtained in *ab initio* calculations of various types [13, 25–29].

In this work, we observe the emergence of collective rotation in *ab initio* NCCI calculations for the Be isotopes, with $7 \leq A \leq 12$, using the realistic JISP16 nucleon-nucleon interaction [30]. Evidence for rotational band structure is found in the calculated excitation energies, electric quadrupole moments, $E2$ transition matrix elements, magnetic dipole moments, and $M1$ transition matrix elements. In calculations of the even-mass Be nuclei, yrast or near-yrast sequences of angular momenta 0, 2, 4, ... arise with calculated properties suggestive of $K = 0$ rotational bands. However, the most distinctive, well-developed, and systematic rotational band structures are observed in calculations for odd-mass nuclei. Given the same range of excitation energies and angular momenta, the low-lying $\Delta J = 1$ bands in the odd-mass nuclei provide a richer set of energy and electromagnetic observables. Bands are identified in both the natural (or valence-space) and unnatural parity spaces.

First, the properties expected in nuclear rotational structure are reviewed, for the observables under consideration (Sec. II). Then, the results for rotational bands in NCCI calculations of these Be isotopes are presented (Sec. III): the calculations are outlined, re-

sults for energies and electromagnetic matrix elements are presented, and convergence is explored. Finally, the calculated energies and electromagnetic observables are examined in the context of rotational band structure, and the calculated rotational bands are compared with experiment (Sec. IV). Preliminary results were reported in Refs. [29, 31].

II. BACKGROUND: ROTATION

A. Rotational states

We first review the nature and expected signatures of nuclear rotation [1, 3, 32]. Under the assumption of adiabatic separation of the rotational degree of freedom, a rotational nuclear state may be described in terms of an *intrinsic state*, as viewed in the non-inertial intrinsic frame, together with the rotational motion of this intrinsic frame. Here we consider, in particular, axially symmetric structure, for which the intrinsic state $|\phi_K\rangle$ is characterized by definite angular momentum projection K along the intrinsic symmetry axis. The full nuclear state $|\psi_{JKM}\rangle$, with total angular momentum J and projection M , then has the form

$$|\psi_{JKM}\rangle = \left[\frac{2J+1}{16\pi^2(1+\delta_{K0})} \right]^{1/2} \int d\vartheta [\mathcal{D}_{MK}^J(\vartheta)|\phi_K;\vartheta\rangle + (-)^{J+K}\mathcal{D}_{M-K}^J(\vartheta)|\phi_{\bar{K}};\vartheta\rangle], \quad (1)$$

where ϑ represents the Euler angles for rotation of the intrinsic state, and $|\phi_{\bar{K}}\rangle$ is the \mathcal{R}_2 -conjugate intrinsic state (the \mathcal{R}_2 operator induces a rotation by π around the intrinsic-frame y axis), which has angular momentum projection $-K$ along the symmetry axis.

The most recognizable features in the spectroscopy of rotational states reside not in the states taken individually but in the relationships — relative energies and electromagnetic multipole operator matrix elements — among different rotational states $|\psi_{JKM}\rangle$ sharing the same intrinsic state $|\phi_K\rangle$. These states constitute members of a rotational band, with angular momenta $J = K, K+1, \dots$, except that, for $K=0$ bands, only even J are present, in the case of positive \mathcal{R}_2 symmetry (or only odd J , in the case of negative \mathcal{R}_2 symmetry).

B. Energies

Within a rotational band, energies follow the pattern

$$E(J) = E_0 + AJ(J+1), \quad (2)$$

where, in terms of the moment of inertia \mathcal{J} about an axis perpendicular to the symmetry axis, the rotational energy constant is $A \equiv \hbar^2/(2\mathcal{J})$. For $K = 1/2$ bands, deviation from the adiabatic rotational energy formula (2) is generally substantial, due to the influence of the Coriolis contribution to the kinetic energy. If one assumes that the intrinsic state may be well-described as a single nucleon coupled to an axially symmetric core, the result is an energy staggering given by

$$E(J) = E_0 + A[J(J+1) + a(-)^{J+1/2}(J + \frac{1}{2})], \quad (3)$$

where a is the Coriolis decoupling parameter.

C. Quadrupole matrix elements

Reduced matrix elements $\langle \psi_{J_f K} \| \mathbf{Q}_2 \| \psi_{J_i K} \rangle$ of the electric quadrupole (E2) operator \mathbf{Q}_2 between states within a band¹ are entirely determined by the intrinsic matrix elements and the rotational structure. These reduced matrix elements are given by [1]

$$\begin{aligned} \langle \psi_{J_f K} \| \mathbf{Q}_2 \| \psi_{J_i K} \rangle = \frac{(2J_i + 1)^{1/2}}{1 + \delta_{K0}} & \left[(J_i K 20 | J_f K) \langle \phi_K | Q_{2,0} | \phi_K \rangle \right. \\ & \left. + (-)^{J_i + K} (J_i, -K, 2, 2K | J_f K) \langle \phi_K | Q_{2,2K} | \phi_{\bar{K}} \rangle \right], \quad (4) \end{aligned}$$

where J_i and J_f are the initial and final angular momenta. The second (or cross) term in (4), involving $\langle \phi_K | Q_{2,2K} | \phi_{\bar{K}} \rangle$, contributes only for $0 \leq K \leq 1$, in which case the quadrupole operator can connect the intrinsic state $|\phi_K\rangle$ with its conjugate state $|\phi_{\bar{K}}\rangle$. For $K = 0$, the contribution of this term is identical to that of the first term, and it therefore simply enters into the normalization of the expression, its effect cancelling that of the $1 + \delta_{K0}$ factor. Let us set aside, for the moment, the possible contribution of this cross term for bands with $K = 1/2$ or 1.

Then, all reduced matrix elements within a band are proportional to the intrinsic quadrupole moment $eQ_0 \equiv (16\pi/5)^{1/2} \langle \phi_K | Q_{2,0} | \phi_K \rangle$, *i.e.*, the quadrupole moment of the

¹ We follow the reduced matrix element normalization and phase conventions of Edmonds [33, 34]. Therefore, quadrupole moments are related to reduced matrix elements by $eQ(J) \equiv (16\pi/5)^{1/2} \langle JJ | Q_{2,0} | JJ \rangle = (16\pi/5)^{1/2} (2J+1)^{-1/2} (JJ20 | JJ) \langle J \| \mathbf{Q}_2 \| J \rangle$, and reduced transition probabilities are related to reduced matrix elements by $B(E2; J_i \rightarrow J_f) = (2J_i + 1)^{-1} |\langle J_f \| \mathbf{Q}_2 \| J_i \rangle|^2$.

intrinsic state, as calculated with respect to the intrinsic symmetry axis. The spectroscopic quadrupole moments of band members are obtained in terms of Q_0 as

$$Q(J) = \frac{3K^2 - J(J+1)}{(J+1)(2J+3)}Q_0, \quad (5)$$

and reduced transition probabilities within a band are obtained as

$$B(E2; J_i \rightarrow J_f) = \frac{5}{16\pi} (J_i K 20 | J_f K)^2 (eQ_0)^2. \quad (6)$$

However, in the present work, rather than considering these reduced transition probabilities, we shall find it more informative to consider the *signed* reduced matrix elements

$$\langle \psi_{J_f K} || \mathbf{Q}_2 || \psi_{J_i K} \rangle = \sqrt{\frac{5}{16\pi}} (2J_i + 1)^{1/2} (J_i K 20 | J_f K) (eQ_0), \quad (7)$$

to retain further meaningful phase information as we examine the rotational structure. The values of $Q(J)$ and $\langle \psi_{J_f K} || \mathbf{Q}_2 || \psi_{J_i K} \rangle$ within a rotational band, normalized to Q_0 , are shown for reference in Fig. 1.

In obtaining these results for rotational matrix elements, \mathbf{Q}_2 may be taken to be any operator of the form $Q_{2\mu} = \sum_{i=1}^A e_i r_i^2 Y_{2\mu}(\hat{\mathbf{r}}_i)$, where e_i is a “charge” for the i th nucleon, and \mathbf{r}_i its position [35]. Depending on the choice of the coefficients e_i for protons and neutrons, \mathbf{Q}_2 may therefore variously represent the proton quadrupole — or physical electric quadrupole — tensor $\mathbf{Q}_p = e \sum_{i=1}^Z r_{p,i}^2 Y_2(\hat{\mathbf{r}}_{p,i})$ (for $e_p = e$ and $e_n = 0$), the neutron quadrupole tensor $\mathbf{Q}_n = e \sum_{i=1}^N r_{n,i}^2 Y_2(\hat{\mathbf{r}}_{n,i})$ (for $e_p = 0$ and $e_n = e$), or the mass quadrupole tensor \mathbf{Q}_m (*i.e.*, their sum).² While matrix elements of the electric quadrupole operator \mathbf{Q}_p are most immediately accessible in experiment, through electromagnetic observables, matrix elements of \mathbf{Q}_n may be viewed on an equal footing in the rotational analysis of calculated wave functions. Therefore, these neutron matrix elements are considered alongside the proton matrix elements throughout Sec. III. They provide a valuable complementary set of observables for the purpose of investigating whether or not the nuclear wave functions satisfy the conditions of adiabatic rotational separation.

² For consistency with common notation in the context of electromagnetic transitions [1], we retain the electron charge e in the normalization for both \mathbf{Q}_p and \mathbf{Q}_n . To the extent that isospin symmetry is maintained, calculations of neutron quadrupole matrix elements in the Be isotopes are equivalent to calculations of electric quadrupole matrix elements for isospin partner states in the $N = 4$ isotones.

Let us now return to the cross term in the rotational expression (4) for the reduced matrix element. In the analysis of $K = 1/2$ or 1 bands in well-deformed rotor nuclei, in heavier mass regions, this cross term is commonly neglected, since $Q_0 \sim \langle \phi_K | Q_{2,0} | \phi_K \rangle$ is strongly enhanced, while $\langle \phi_K | Q_{2,2K} | \phi_{\bar{K}} \rangle$ is presumed to be of typical single-particle strength [1]. However, it may have greater significance for the light nuclei considered here, where the number of nucleons participating in collective motion is more limited, and rotational quadrupole strengths for candidate rotational states can therefore be expected to be less dramatically enhanced over single-particle strengths.

The alternating sign of the cross term, for successive J_i values, may therefore be expected to introduce a nonnegligible staggering in matrix elements for bands with $K = 1/2$ or 1. That said, for the particular case of quadrupole moments (diagonal matrix elements) in $K = 1/2$ bands, of principal interest in the present work, it should be noted that the cross term does not actually contribute to the rotational predictions, since the Clebsch-Gordan coefficients $(J - \frac{1}{2} 2 1 | J \frac{1}{2})$ vanish identically, and thus no staggering is obtained. The cross-term can still induce staggering in the transition matrix elements within these $K = 1/2$ bands. For illustration, the staggering induced by intrinsic matrix elements in the ratio $\langle \phi_K | Q_{2,2K} | \phi_{\bar{K}} \rangle / \langle \phi_K | Q_{2,0} | \phi_K \rangle = +0.1$ is indicated in Fig. 1(b) (see dotted curves). Staggering of approximately this scale may be suggested by (or is at least not inconsistent with) some of the calculated results for matrix elements in Sec. III C.

D. Dipole matrix elements

The standard rotational analysis for magnetic dipole (M1) matrix elements [1, 3] relies upon the assumption that the nucleus may be divided into a “core” rotor and extra-core particles. First, we recall that the magnetic dipole operator may be written as

$$\mathbf{M}_1 = \sqrt{\frac{3}{4\pi}} \mu_N \sum_{i=1}^A (g_{\ell,i} \boldsymbol{\ell}_i + g_{s,i} \mathbf{s}_i), \quad (8)$$

where μ_N is the nuclear magneton, $g_{\ell,i}$ and $g_{s,i}$ are the orbital and spin g -factors for the i th nucleon, $\boldsymbol{\ell}_i$ and \mathbf{s}_i are the dimensionless orbital and spin angular momentum operators, and we have adopted Gaussian units [35]. Then a decomposition of the dipole operator into core and particle terms is accomplished as $\mathbf{M}_1 = [3/(4\pi)]^{1/2} g_R \mu_N \mathbf{J} + \mathbf{M}'_1$, where g_R is an effective gyromagnetic ratio for the core rotor, \mathbf{J} is the dimensionless total angular

momentum operator, and $\mathbf{M}'_1 = [3/(4\pi)]^{1/2} \mu_N \sum_{i=1}^A [(g_{\ell,i} - g_R)\boldsymbol{\ell}_i + (g_{s,i} - g_R)\mathbf{s}_i]$. The matrix elements of the first term include the entire contribution of the core rotor. Matrix elements of the second, residual term \mathbf{M}'_1 receive contributions only from the extra-core particles. The rotational predictions for these latter matrix elements may be expressed in terms of intrinsic matrix elements, much as for the quadrupole operator in (4).

Reduced matrix elements³ of the full magnetic dipole operator between states within a band are given by [1]

$$\begin{aligned} \langle \psi_{J_f K} \| \mathbf{M}_1 \| \psi_{J_i K} \rangle &= g_R \mu_N \langle J_f \| \mathbf{J} \| J_i \rangle \delta_{J_i J_f} + (2J_i + 1)^{1/2} \left[(J_i K 1 0 | J_f K) \langle \phi_K | M'_{1,0} | \phi_K \rangle \right. \\ &\quad \left. + \delta_{K, \frac{1}{2}} (-)^{J_i + \frac{1}{2}} (J_i - \frac{1}{2} 2 1 | J_f \frac{1}{2}) \langle \phi_{1/2} | M'_{1,1} | \phi_{\overline{1/2}} \rangle \right]. \quad (9) \end{aligned}$$

The first (rotor) term contributes only to the diagonal matrix elements, *i.e.*, with $J_f = J_i$, for which case we may use the standard identity for the reduced matrix element of the angular momentum operator within a state of angular momentum J , $\langle J \| \mathbf{J} \| J \rangle = [J(J+1)(2J+1)]^{1/2}$. The first (or direct) term within the brackets, involving the matrix element $\langle \phi_K | M'_{1,0} | \phi_K \rangle$, contributes in general (except for $K = 0$ dipole moments), while the second (or cross) term within the brackets, involving the matrix element $\langle \phi_{1/2} | M'_{1,1} | \phi_{\overline{1/2}} \rangle$ between conjugate intrinsic states, contributes only for $K = 1/2$. In this case, the cross term may contribute with a strength comparable to that of the direct term [3].

For later reference, in Sec. III C, we note the explicit forms of the rotational predictions which are obtained from (9), after evaluating the Clebsch-Gordan coefficients (*e.g.*, Sec. 8.5 of Ref. [34]). For dipole moments,

$$\mu(J) = a_0 J + a_1 \frac{K}{J+1} + a_2 \delta_{K, \frac{1}{2}} \frac{(-)^{J-1/2}}{2\sqrt{2}} \frac{2J+1}{J+1}, \quad (10)$$

and, for the reduced matrix elements for $\Delta J = 1$ transitions,

$$\langle \psi_{J-1, K} \| \mathbf{M}_1 \| \psi_{J K} \rangle = -\sqrt{\frac{3}{4\pi}} \sqrt{\frac{J^2 - K^2}{J}} \left[a_1 + a_2 \delta_{K, 1/2} \frac{(-)^{J-1/2}}{\sqrt{2}} \right], \quad (11)$$

where $a_0 = g_R \mu_N$, $a_1 = (4\pi/3)^{1/2} \langle \phi_K | M'_{1,0} | \phi_K \rangle$, and $a_2 = (4\pi/3)^{1/2} \langle \phi_{1/2} | M'_{1,1} | \phi_{\overline{1/2}} \rangle$. The terms contributing to $\mu(J)$ in (10) are shown in Fig. 2(a), while those contributing to $\langle \psi_{J-1, K} \| \mathbf{M}_1 \| \psi_{J K} \rangle$ in (11) are shown in Fig. 2(b).

³ Under the present reduced matrix element convention (see footnote 1), dipole moments are related to reduced matrix elements by $\mu(J) \equiv (4\pi/3)^{1/2} \langle J J | M_{1,0} | J J \rangle = (4\pi/3)^{1/2} (2J+1)^{-1/2} \langle J J 1 0 | J J \rangle \langle J \| \mathbf{M}_1 \| J \rangle$, and reduced transition probabilities by $B(M1; J_i \rightarrow J_f) = (2J_i + 1)^{-1} |\langle J_f \| \mathbf{M}_1 \| J_i \rangle|^2$.

In obtaining these results for rotational matrix elements, \mathbf{M}_1 may be any operator of the form (8). The structure of this operator is more apparent if it is decomposed into proton/neutron and orbital/spin contributions, as

$$\mathbf{M}_1 = g_{\ell,p} \mathbf{D}_{\ell,p} + g_{\ell,n} \mathbf{D}_{\ell,n} + g_{s,p} \mathbf{D}_{s,p} + g_{s,n} \mathbf{D}_{s,n}, \quad (12)$$

where we define the *dipole terms*⁴

$$\mathbf{D}_{\ell,p} = \sqrt{\frac{3}{4\pi}} \mu_N \boldsymbol{\ell}_p \quad \mathbf{D}_{\ell,n} = \sqrt{\frac{3}{4\pi}} \mu_N \boldsymbol{\ell}_n \quad \mathbf{D}_{s,p} = \sqrt{\frac{3}{4\pi}} \mu_N \mathbf{s}_p \quad \mathbf{D}_{s,n} = \sqrt{\frac{3}{4\pi}} \mu_N \mathbf{s}_n, \quad (13)$$

where $\boldsymbol{\ell}_p$ is the total proton orbital angular momentum operator [$\boldsymbol{\ell}_p \equiv \sum_{i=1}^Z \boldsymbol{\ell}_{p,i}$], $\boldsymbol{\ell}_n$ is the total neutron orbital angular momentum operator [$\boldsymbol{\ell}_n \equiv \sum_{i=1}^N \boldsymbol{\ell}_{n,i}$], \mathbf{s}_p is the total proton spin angular momentum operator [$\mathbf{s}_p \equiv \sum_{i=1}^Z \mathbf{s}_{p,i}$], and \mathbf{s}_n is the total neutron spin angular momentum operator [$\mathbf{s}_n \equiv \sum_{i=1}^N \mathbf{s}_{n,i}$]. The electromagnetic $M1$ operator is obtained for the particular choice $g_{\ell,p} = 1$, $g_{\ell,n} = 0$, $g_{s,p} \approx 5.586$, and $g_{s,n} \approx -3.826$. However, the rotational results (10)–(11) apply more generally to matrix elements of any linear combination of these terms, including, as we shall consider in Sec. III, each of the four dipole terms individually.

These different dipole operators provide complementary probes of the proton/neutron and orbital/spin contributions to the rotational structure.⁵ Thus, while matrix elements of the traditional electromagnetic $M1$ operator are most immediately accessible in experiment, they do not exhaust the available structural information for calculated wave functions. For instance, the electromagnetic operator is blind to the neutron orbital motion, which may be expected to be a dominant contributor to total angular momentum in a neutron-rich rotational nucleus.

⁴ In, *e.g.*, Ref. [35], the expression *dipole term* is used to refer to each of the contributing proton/neutron and orbital/spin *matrix elements*, when the $M1$ operator is applied at the one-body level, *i.e.*, between single-particle orbitals. Here we generalize the use of *dipole term* to refer to each of the contributing proton/neutron and orbital/spin *operators*, and to the application of these operators at the many-body level.

⁵ In particular, the diagonal matrix elements, or dipole moments, calculated using each of the individual dipole terms are proportional to the $\boldsymbol{\ell}_p$, \mathbf{s}_p , $\boldsymbol{\ell}_n$, and \mathbf{s}_n contributions, respectively, to the total angular momentum of the nuclear state [36] (see also Sec. IV B).

III. RESULTS

A. Calculations

We consider here the results of NCCI calculations for the Be isotopes with $7 \leq A \leq 12$. In practice, nuclear many-body calculations must be carried out in a truncated space. A conventional harmonic oscillator basis is used for the present calculations, with truncation according to the N_{max} scheme, that is, by the number of oscillator excitations relative to the lowest Pauli-allowed configuration. The eigenvalues and wave functions, and thus calculated observables, obtained in such calculations are in general dependent both upon the basis truncation N_{max} and on the oscillator length for the basis, which is specified by the oscillator energy $\hbar\Omega$. Detailed illustrations may be found in, *e.g.*, Refs. [16, 23, 24, 36, 37], including calculations for some of the isotopes and observables under consideration here. In the present calculations, basis truncations $N_{\text{max}} = 10$ or 11 have been used, depending on the parity under consideration, as discussed further below. The basis $\hbar\Omega$ parameters have been chosen near the variational minimum for the ground state energy (specifically, $\hbar\Omega = 20$ MeV for ${}^7,8\text{Be}$ and $\hbar\Omega = 22.5$ MeV for ${}^9\text{--}^{12}\text{Be}$). The calculations are carried out in the proton-neutron M scheme [38], using the code MFDn [39–41].

These calculations are based on the JISP16 interaction [30], which is a charge-independent two-body interaction derived from neutron-proton scattering data and adjusted via a phase-shift equivalent transformation to describe light nuclei without explicit three-body interactions. The bare JISP16 interaction is used, without renormalization to the truncated space (see Ref. [16]). The Coulomb interaction has been omitted from the Hamiltonian, to ensure exact conservation of isospin, thereby simplifying the spectrum (we consider states of minimal isospin $T = T_z$). However, the primary effect of the Coulomb interaction, if included, is simply to induce a shift in the overall binding energies, which is irrelevant to the analysis of rotational band observables.

Due to the parity conserving nature of the nuclear interaction in these calculations, the eigenproblem separates into positive and negative parity sectors. The parity of the lowest allowed oscillator configuration may be termed the *natural parity*, and that obtained by promoting one nucleon by one shell the *unnatural parity*. Thus, the natural parity is negative for the odd-mass isotopes ${}^7,9,11\text{Be}$, and positive for the even-mass isotopes ${}^8,10,12\text{Be}$. While

the lowest unnatural parity states normally lie at significantly higher energy than those of natural parity, they are calculated to lie within a few MeV of the lowest natural parity states in the isotopes $^9,^{11}\text{Be}$ [29], and are thus included in the present discussion of these nuclei. Note that parity inversion arises for ^{11}Be , *i.e.*, the ground state is experimentally [42] in the unnatural parity space, and both spaces are near-degenerate in calculations at finite N_{max} (see Ref. [22]). The NCCI basis states with an even number of excitations above the lowest oscillator configuration span the natural parity space, while the basis states with an odd number of excitations span the unnatural parity space, hence the application of even and odd N_{max} truncations to these spaces, respectively.

Diagonalization of the large Hamiltonian matrices encountered in these NCCI calculations relies upon the Lanczos algorithm [43]. For a given number of Lanczos iterations, only a limited set of energy eigenvalues (and corresponding eigenvectors) are converged, starting from the bottom of the spectrum, giving the lowest energies within the given many-body space. Within the framework of an M -scheme calculation, where many-body basis states are restricted to a given value of the total angular momentum projection M , all states with $J \geq M$ are included in the space (*e.g.*, Ref. [38]). Thus, in practice, to address the entire yrast region, results of calculations in spaces with different M values must be aggregated. For example, the yrast state of a given J might be too high in the energy spectrum to be practically obtained from calculations in the $M = 0$ space (or $M = 1/2$ for odd-mass nuclei). However, in the $M = J - 2$ space, this lowest state of angular momentum J might be one of the highest states actually converged (the 20th, say). And, in the $M = J$ space, it may be expected to be one of the lowest states obtained (albeit not necessarily *the* lowest, since the yrast line is not necessarily monotonic, particularly in the presence of Coriolis staggering).

B. Energy levels

Identification of candidate rotational band members relies not only on recognizing rotational energy patterns, but also on identifying collective enhancement of quadrupole transition strengths and verifying rotational patterns of electromagnetic moments and transition matrix elements. Nonetheless, it is natural to begin the discussion of band structure by considering energies.

The calculated energy eigenvalues for low-lying states of the odd-mass Be isotopes (with

$7 \leq A \leq 11$) are shown in Fig. 3. Where both natural and unnatural parity spaces have been calculated (see Sec. III A), these are shown separately. Low-lying states of even-mass Be isotopes (with $8 \leq A \leq 12$) are shown in Fig. 4. To facilitate identification of rotational bands, it is helpful to plot the calculated excitation energies against an angular momentum axis which is scaled as $J(J+1)$, so that energies within an ideal rotational band lie on a straight line or, for $K = 1/2$ bands, staggered about a straight line. For the candidate bands in Figs. 3 and 4, a straight line fit (2) to all band members is shown, except that, for $K = 1/2$ bands, an energy fit is obtained by adjusting the parameters of (3) to the lowest three band members (the remainder of the line is thus an extrapolation).

The yrast states are noticeably isolated in energy from the remaining states at low angular momentum, though not necessarily at the higher angular momenta shown in Figs. 3 and 4. This separation is by ~ 20 MeV for the ground state of ^8Be [Fig. 4(a)]. The yrast and near-yrast states therefore yield the most immediately recognizable sets of candidate band members. Candidate yrast band members, in particular, are indicated by the solid black squares in Figs. 3 and 4. The yrast band members can, for the most part, be identified simply from the rotational pattern of their energies, although in the present analysis the energy is taken only as a basis for identification of *candidate* band members, pending further analysis of electromagnetic observables. “Yrast” bands may be identified separately in the natural [Fig. 3(a,b,d)] and unnatural [Fig. 3(c,e)] parity spaces. In the odd-mass Be isotopes considered (Fig. 3), yrast rotational bands are found with $K = 1/2$ or $3/2$. In the even-mass Be isotopes, the yrast states (Fig. 4) constitute prospective $K = 0$ ground state rotational bands, albeit in some instances severely truncated.

The density of states rapidly increases off the yrast line, leading to the possibility of fragmentation of rotational states by mixing with nearby states and, in general, hindering the identification of band members. For the yrast $K = 1/2$ bands, alternate bandmembers are raised in energy into this region of higher density of states, as a result of the Coriolis staggering in energies. Any excited bands must also be sought in this region of higher density of states. Nonetheless, several excited candidate bands can be identified,⁶ once

⁶ We focus, in the present discussion, on the most clearly identifiable yrast or near-yrast bands. However, this should not be taken to exclude the possibility of additional excited bands, suggestions of which may be found in the calculated spectra and matrix elements. See, *e.g.*, Fig. 2(b) of Ref. [31], for a low-lying example.

electromagnetic moments and transition matrix elements have been taken into account, as indicated by shaded squares in Figs. 3 and 4. Excited candidate bands are identified in the natural parity spaces of ^9Be [Fig. 3(b)], ^{11}Be [Fig. 3(d)], ^{10}Be [Fig. 4(b)], and ^{12}Be [Fig. 4(c)], again with $K = 1/2$ or $3/2$ for the odd-mass isotopes, or $K = 0$ for the even-mass isotopes. Examples of fragmentation of rotational candidate band members, as indicated by quadrupole transition strengths, may be seen in the present calculations at $J = 2$ in the excited band of ^{10}Be [Fig. 4(b)] and at $J = 11/2$ in the unnatural parity yrast band of ^{11}Be [Fig. 3(e)].

A basic question to be addressed (taken up in view of the full set of calculated data in Sec. IV A) is whether or not the rotational bands exhibit termination. If so, we then wish to understand the relation between the terminating angular momentum and the angular momenta accessible in a traditional valence shell description for these nuclei. In general, the maximal angular momentum available in the $N_{\text{max}} = 0$ space, *i.e.*, the lowest oscillator configuration, of the NCCI scheme is, equivalently, the maximal angular momentum possible in a traditional shell model description using the last partially-occupied oscillator shell (here the p shell) as the valence space. This maximal valence angular momentum is indicated by the dashed vertical lines in Figs. 3 and 4. For the unnatural parity spaces [Fig. 3(c,e)], the maximal angular momentum accessible in the $N_{\text{max}} = 1$ space, *i.e.*, the lowest oscillator configuration of *unnatural* parity, is indicated instead. This angular momentum is, in general, higher than for the corresponding natural parity space, since promotion of a nucleon to a higher shell relaxes Pauli constraints on the allowed angular momentum couplings, while also making higher- j orbitals accessible. The maximal angular momenta are summarized in Table I.

Candidate yrast bands in Figs. 3 and 4 exhibit some form of discontinuity in the evolution of the energies with J , or else clear termination, at the maximal valence angular momentum. In contrast, several of the excited candidate bands extend to higher angular momentum without apparent disruption to the rotational energy pattern. These observations are revisited below (Sec. IV A) in light of electromagnetic observables.

C. Electromagnetic matrix elements

For each candidate rotational band highlighted in Figs. 3 and 4, we now compare the calculated electric quadrupole and magnetic dipole matrix elements — that is, moments and transition matrix elements — with the rotational predictions. The calculated results are shown in Figs. 5–11 for the odd-mass Be isotopes and in Figs. 12–15 for the even-mass Be isotopes.⁷ Let us for now focus on defining the contents of these figures, while deferring analysis to Sec. IV.

In each of Figs. 5–15, the quadrupole moments for all states within the considered band are shown in panel (a). The values are normalized to Q_0 , to facilitate uniform comparison with the rotational predictions for $Q(J)/Q_0$ from (5), which are shown as a curve in each plot, appropriate to the K quantum number of the given band. The value of Q_0 used for normalization has in each case been obtained simply from the quadrupole moment of the lowest-energy bandmember with nonvanishing quadrupole moment. Thus, for $K = 1/2$ bands, since the quadrupole moment of the $J = 1/2$ band head vanishes identically, either the $J = 3/2$ or $5/2$ band member is used for normalization, according to the energy staggering. Similarly, for $K = 0$ bands, the quadrupole moment of the $J = 2$ band member is used for normalization. The exceptions are the excited $K = 0$ bands in ^{10}Be [Fig. 14(a)] and ^{12}Be [Fig. 15(a)], for which the $J = 4$ band member is found to be less fragmented and therefore used for normalization. Quadrupole moments in Figs. 5–15 are calculated using both the proton (filled symbols) and neutron (open symbols) quadrupole tensors (as discussed in Sec. II C). (In some cases, data points for the neutron results may not be separately visible in these figures, when they are indistinguishable from the corresponding proton results.) The proton and neutron quadrupole moments are normalized separately, since no *a priori* relation exists between the intrinsic matrix elements of the \mathbf{Q}_p and \mathbf{Q}_n operators (except in ^8Be , where isospin symmetry makes the proton and neutron quadrupole moments trivially identical).

In-band quadrupole transition reduced matrix elements are shown in panel (b) of each of Figs. 5–15, again as obtained for both proton (solid symbols) and neutron (open symbols) quadrupole operators, and for $\Delta J = 2$ transitions (upper curves) and $\Delta J = 1$ transitions

⁷ The radically truncated $K = 0$ yrast band of ^{12}Be , which terminates at $J = 2$, as indicated in Fig. 4(c), is not included among these figures but does appear in Sec. IV.

(lower curves), with the latter not being applicable to $K = 0$ bands [Figs. 12–15]. The matrix elements are shown normalized as $\langle J - \Delta J \| \mathbf{Q}_2 \| J \rangle / (eQ_0)$, for comparison with rotational values from (7). The same Q_0 values are used as in panel (a) of each of the figures, *i.e.*, deduced from the quadrupole moment of a suitable low-lying band member. Therefore, no free normalization parameter remains for the transition matrix elements in panel (b). For $K = 1/2$ bands, recall that the quadrupole moments are insensitive to the cross term connecting \mathcal{R}_2 -conjugate intrinsic states in (4) and therefore cannot be used to extract the corresponding intrinsic matrix element $\langle \phi_K | Q_{2,2K} | \phi_{\bar{K}} \rangle$. No attempt is made to “fit” any possible staggering in the calculated quadrupole transition matrix elements to determine this matrix element. Rather, the rotational values of matrix elements from (7) are simply shown, without the cross term, as a baseline for any possible staggering.

The four distinct “dipole moments” for each band member, calculated using each of the separate dipole term operators $\mathbf{D}_{\ell,p}$, $\mathbf{D}_{\ell,n}$, $\mathbf{D}_{s,p}$, and $\mathbf{D}_{s,n}$ (defined in Sec. IID) are shown in panel (c) of each of Figs. 5–15. Similarly, for the odd-mass Be isotopes, the four distinct $\Delta J = 1$ dipole transition matrix elements, calculated using each of the dipole term operators, are shown in panel (d) of each of Figs. 5–11. (No dipole transitions are possible in the $K = 0$ bands of the even-mass Be isotopes, due to the $\Delta J = 2$ angular momentum difference between levels.) The magnetic dipole moment or magnetic dipole transition matrix element pertinent to physical electromagnetic transitions can, of course, be recovered as a particular linear combination (12) of these values, as determined by the physical g factors (Sec. IID). However, for purposes of rotational analysis, we retain the more complete information provided by the matrix elements of the four physically distinct dipole terms.

The rotational predictions for the dipole moments from (10) involve up to three parameters (a_0 , a_1 , and a_2), representing the different core rotor and intrinsic matrix elements, in contrast to the situation for the quadrupole moments, for which the rotational predictions have as their only parameter a simple overall normalization. As noted in Sec. IID, the cross term may contribute with a strength comparable to that of the direct term, so no simplification can be obtained through its omission. Similarly, the rotational predictions for the dipole transitions involve up to two parameters (a_1 and a_2). Therefore, the calculated values are shown directly in Figs. 5–15, without normalization to any fitted intrinsic matrix element.

The curves representing the rotational predictions are thus not uniquely determined by the K quantum number but rather are determined by a simultaneous global fit of the parameters a_0 , a_1 , and a_2 (as applicable, depending upon the K quantum number) to the dipole moments and transition matrix elements (again, as applicable) within the band. For $K = 0$ bands, the expected angular momentum dependence for the dipole moments is indeed simply linear, and the fit consists of determining the core rotor normalization parameter a_0 . For $K = 1/2$ bands, all three terms (involving a_0 , a_1 , and a_2) are involved, introducing staggering, while, of these, only the two involving a_1 and a_2 enter into the expected transition matrix elements. Finally, for bands with $K > 1/2$, only two terms (involving a_0 and a_1) are in play, while only the term involving a_1 enters into the expected transition matrix elements. These parameters for the rotational predictions are fitted independently for each of the dipole term operators, within a band, as there is no *a priori* relation among the intrinsic matrix elements for the different dipole terms. These fits give equal weights to all moments and transitions, where all levels within the band are considered up to the point at which substantial anomalies (band termination) or fragmentation effects are found to occur.

Recall that our purpose is to determine the extent to which the calculated eigenstates in the *ab initio* calculation conform to the expectation of an adiabatic rotational scheme, *i.e.*, one yielding wave functions of the form (1), and that, to do so, we are relying upon the indirect evidence provided by energies and matrix elements of electromagnetic operators — these latter, the matrix elements, being concretely related to the hypothesized form (1) for the wave functions. Since *signed* reduced matrix elements $\langle J_f || \mathbf{T}_\lambda || J_i \rangle$, rather than *unsigned* reduced transition probabilities $B(T\lambda; J_i \rightarrow J_f)$, of a transition operator \mathbf{T}_λ , are considered — for both quadrupole and dipole transitions — in Figs. 5–15, it is necessary for us to elaborate on the extraction of the signs on these quantities and their interpretation in the rotational context. The rotational predictions for the matrix elements — as given in (4) and (9) — entail definite relations among the signs of the transition matrix elements (which are also related to the signs of the moments). These signs are lost (through taking the square) in going from matrix elements to transition probabilities. When comparing with experiment, such loss of sign information is inconsequential, since the signs of transition matrix elements are impossible to extract experimentally (a possible exception, in principle, being through interference between different excitation pathways in multi-step Coulomb excitation [44]). However, the relevant matrix elements are fully accessible for the present

ab initio calculated wave functions.

In considering the signs of calculated matrix elements, it must be borne in mind that the eigenfunctions of the Hamiltonian are determined only to within an overall phase (*i.e.*, sign, for real wave functions). Thus, if the state $|\psi_{JKM}\rangle$ of (1) is characterized by a rotational wave function, then $-|\psi_{JKM}\rangle$ is an equally valid rotational state — the choice of one over the other being simply a matter of convention, implicitly embodying also the arbitrary choices of convention entailed in the definitions of the \mathcal{D} functions and Clebsch-Gordan coefficients [33]. Numerical diagonalization of the many-body Hamiltonian will arbitrarily select either sign for the eigenvector (in general, irreproducibly, depending upon the choice of initial Lanczos trial states or other variations in algorithmic details). Diagonal matrix elements (or moments) are insensitive to the sign of the wave function. The sign choices on two states of angular momenta J and J' — which we may denote by σ_J and $\sigma_{J'}$, respectively — enter into the transition reduced matrix elements $\langle J' || \mathbf{T}_\lambda || J \rangle$ between these states as the product $\sigma_{J'}\sigma_J$.

In comparing the results for matrix elements from the calculated eigenvectors with the values expected from the rotational model formulas, one must therefore attempt to choose the phases on the calculated eigenvectors to best correlate with the phase convention embodied in (1). The present analysis considers matrix elements of a multitude of operators among the states within a band, which suffice to fully determine (or, rather, overdetermine) the comparatively few arbitrary phase choices arising from the signs on the states. For instance, if we consider specifically the transitions among three adjacent band members of angular momenta $J-2$, $J-1$, and J , there are 14 independent transition reduced matrix elements considered in this work, namely, four from the $\Delta J = 1$ transitions for the two independent quadrupole operators (\mathbf{Q}_p and \mathbf{Q}_n), two more from the $\Delta J = 2$ transitions for these quadrupole operators, and eight from the $\Delta J = 1$ transitions for the four independent dipole operators ($\mathbf{D}_{\ell,p}$, $\mathbf{D}_{\ell,n}$, $\mathbf{D}_{s,p}$, and $\mathbf{D}_{s,n}$):

$$\begin{array}{ccccc} J-2 & \xleftarrow{2E2+4M1} & J-1 & \xleftarrow{2E2+4M1} & J \\ \bigcirc & & \bigcirc & & \bigcirc \\ & \xleftarrow{2E2} & & & \end{array}.$$

The transition matrix elements are insensitive to a global reversal of sign, *i.e.*, of σ_{J-2} , σ_{J-1} , and σ_J simultaneously. Thus, effectively, only two arbitrary sign degrees of freedom are present — these may be taken as the choices of the relative phases σ_{J-2}/σ_J and σ_{J-1}/σ_J

of the band members — amongst the signs of the 14 transition matrix elements. The two arbitrary signs may be determined by matching the signs of two transition matrix elements to the signs expected from the rotational formulas: *e.g.*, once the sign of $Q_{0,p}$ has been determined from the quadrupole moments, we may choose the two relative phases σ_{J-2}/σ_J and σ_{J-1}/σ_J so that the $\Delta J = 2$ and $\Delta J = 1$ proton quadrupole transition matrix elements from the state J to the lower band members match those of the rotational predictions. Then, the signs of the remaining 12 matrix elements serve as unambiguous predictions from the many-body calculation, to be tested against the rotational expectations. To allow consistent presentation of signs over the different sets of calculations in Figs. 5–15, the free signs in the transition analysis are chosen to enforce consistency with the positive sign of $Q_{0,p}$ from the quadrupole moment analysis, *i.e.*, to make $\langle J-1 || \mathbf{Q}_{2,p} || J \rangle / (eQ_{0,p})$ negative and/or $\langle J-2 || \mathbf{Q}_{2,p} || J \rangle / (eQ_{0,p})$ positive [see Fig. 1(b)], as applicable.

D. Convergence

The calculations presented in the preceding sections are obtained at a particular level of truncation ($N_{\max} = 10$ or 11) of the many-body configuration space and therefore represent a snapshot along the path to convergence, *i.e.*, to the actual predictions of the many-body Schrödinger eigenproblem with the JISP16 interaction. Therefore, in interpreting the results, it is important to have insight into the nature of the dependence on N_{\max} exhibited by observables for the rotational states, and therefore into the impact of incomplete convergence on the rotational features observed in the calculations.

We focus on ^9Be for illustration, beginning with the energies within rotational bands. Let us first consider the energy eigenvalues (these eigenvalues represent the total binding of the nuclear system). The calculated eigenvalues for several successive values of N_{\max} are shown at top in Fig. 16, both for the natural parity space ($N_{\max} = 6, 8$, and 10) [Fig. 16(a)] and for the unnatural parity space ($N_{\max} = 7, 9$, and 11) [Fig. 16(b)]. For each of these N_{\max} values, the curves indicate rotational formula fits to the energies, obtained as described in Sec. III B. For each step in N_{\max} , it may be observed that the energies shift lower by several MeV, an amount which is large compared to the rotational energy scale. Thus, naively, the energies would seem inadequately converged to permit an analysis of rotational properties.

Nevertheless, the energies of different members of the same band may be observed to

converge at similar rates, and thus the *relative energies* of levels within a band are far less dependent upon the truncation than are the energy eigenvalues themselves. Excitation energies for ${}^9\text{Be}$ are shown at bottom in Fig. 16. (These are calculated separately for each parity, *i.e.*, relative to the “ground state” of that parity.) In examining the unnatural parity band [Fig. 16(d)], it may be noted that there are candidate band members at $J = 15/2$ and $17/2$, above the maximal angular momentum permitted by the valence configuration (Sec. III B), with energies which lie substantially above the rotational energy predictions (by ~ 10 MeV, for $N_{\text{max}} = 11$). However, if we consider the N_{max} dependence, we see that these band members are also falling rapidly in energy relative to lower band members. Thus, as convergence continues, the discontinuity in the behavior of the energies at the maximal valence angular momentum may be substantially altered, perhaps even disappearing, in what would constitute a qualitative change to the band properties from those observed at lower N_{max} values.

While the *excitation energy* of the excited natural parity band of ${}^9\text{Be}$ [Fig. 16(c)], as measured relative to the yrast band, decreases with N_{max} , this relative motion is less rapid than that of the eigenvalues themselves. The change in excitation energy for successive steps in N_{max} is decreasing, suggesting that the excitation energy of the band might be approaching a converged value.

The calculated quadrupole matrix elements are highly dependent on both N_{max} and $\hbar\Omega$,⁸ and at present no definitive procedure is available for extracting estimates for the true, converged values. Nonetheless, *ratios* of calculated quadrupole matrix elements within a band are sufficiently stable with respect to N_{max} to permit identification of the rotational patterns. Again, ${}^9\text{Be}$ is taken for illustration, at top in Fig. 17, where the quadrupole moments of the natural parity [Fig. 17(a)] and unnatural parity [Fig. 17(b)] yrast bands are shown, for successive values of N_{max} . As in Figs. 5–15, these values are taken in ratio to the intrinsic quadrupole moment, which is calculated from the quadrupole moment of the lowest possible band member (see Sec. III C) in each case. The calculated ratios are extremely stable with respect to N_{max} for the lowest band members. Note especially the proton and neutron quadrupole moments of the natural parity $J = 5/2$ band members in

⁸ For representative examples of the N_{max} and $\hbar\Omega$ dependence of calculated quadrupole moments and transition strengths in a neighboring nuclide, see Fig. 9 of Ref. [36]. Results are shown for states in ${}^7\text{Li}$, the mirror nucleus to ${}^7\text{Be}$.

Fig. 17(a). These values remain stable with N_{\max} even though they deviate noticeably from the rotational predictions, so stability is not to be taken to be uniquely associated with strict adiabatic rotation. Greater N_{\max} dependence is found for some of the band members at higher angular momentum.

Convergence of magnetic dipole matrix elements is much more rapid than for electric quadrupole matrix elements. The magnetic dipole moments and transition matrix elements are much less sensitive to the basis $\hbar\Omega$.⁹ The calculated magnetic dipole matrix elements for successive values of N_{\max} are shown in Fig. 17 (bottom). Note that these dipole moments are virtually insensitive to N_{\max} . In the unnatural parity band [Fig. 17(d)], recall that the energy convergence properties change markedly for the band members above the maximal valence angular momentum, but no such discontinuity is observed for the magnetic dipole moments, for which good convergence — and agreement with the rotational fit — is maintained for all candidate band members.

Finally, let us return to the quadrupole moments, but consider them now on an absolute scale (*i.e.*, not as ratios, or normalized to an intrinsic quadrupole moment), despite their poorly converged values. Since the ratios within the bands have already been seen to be largely independent of N_{\max} , the absolute values may be summarized by the overall normalization, as given by the intrinsic quadrupole moment. The intrinsic quadrupole moments, as extracted for each of the bands we are considering in the Be isotopes, from calculations with successive values of N_{\max} (again, $N_{\max} = 6, 8$, and 10 for natural parity bands, or $N_{\max} = 7, 9$, and 11 for unnatural parity bands) are indicated in Fig. 18. Successive N_{\max} calculations for a given band are joined by a line, and the value calculated at the highest N_{\max} is indicated by the largest symbol.

While the absolute magnitudes of $Q_{0,p}$ and $Q_{0,n}$ are far from converged in these calculations, they are increasing with N_{\max} (as is typically the case for NCCI calculations carried out near the variational minimum in $\hbar\Omega$), and they may therefore be interpreted, at least heuristically, as providing a lower bound on the true converged values. The calculated values are already ~ 2 to 10 times a single-particle estimate for the intrinsic quadrupole moment obtained following Weisskopf's approach [45] (see Appendix A for the derivation).

⁹ For the N_{\max} and $\hbar\Omega$ dependence of the calculated dipole moments for several states in ${}^9\text{Be}$, see Fig. 6 of Ref. [36]. The quantities labeled in that figure as spin contributions are equivalent to the dipole terms considered here.

This single-particle estimate varies from $\sim 2.8 \text{ efm}^2$ for $A = 7$ to $\sim 4.1 \text{ efm}^2$ for $A = 12$, as indicated by the shaded bands in Fig. 18.¹⁰

By comparison, although the available experimental electromagnetic moment and transition data for the Be isotopes [42, 46, 47] are limited, we may estimate values for the electric (*i.e.*, proton) intrinsic quadrupole moment $eQ_{0,p}$ from data for the yrast bands of $^8\text{--}^{10}\text{Be}$ using the rotational relations (5) and (6). The low-lying states in ^8Be decay primarily to alpha particles, and the $2^+ \rightarrow 0^+$ gamma-ray branch in the ^8Be yrast band is not observed [47]. However, the measured $4^+ \rightarrow 2^+$ gamma width [48] implies $eQ_{0,p} = 23.0(15) \text{ efm}^2$ for this band.¹¹ The measured $3/2^-$ ground state quadrupole moment in the ^9Be yrast band [47] implies $eQ_{0,p} = 26.44(19) \text{ efm}^2$ for this band. The $5/2^- \rightarrow 3/2^-$ and $7/2^- \rightarrow 3/2^-$ gamma widths [47] are then approximately consistent with the expected rotational values. Specifically, taking the evaluated widths and $E2/M1$ division for the transitions in ^9Be [47] yields $B(E2; 5/2^- \rightarrow 3/2^-)/(eQ_{0,p})^2 = 4.0(3) \times 10^{-2}$, compared to the rotational value $\approx 3.41 \times 10^{-2}$, and $B(E2; 7/2^- \rightarrow 3/2^-)/(eQ_{0,p})^2 = 1.4(6) \times 10^{-2}$, compared to the rotational value $\approx 1.42 \times 10^{-2}$. The measured $2^+ \rightarrow 0^+$ gamma width in the ^{10}Be yrast band [47] implies $eQ_{0,p} = 23.0(11) \text{ efm}^2$ for this band.

Note that, as N_{max} increases, the *ratio* of the proton and neutron intrinsic quadrupole moments remains approximately constant, as may be seen by observing that successive calculated points move approximately radially outward from the origin of the plot, along a line of fixed $Q_{0,p}/Q_{0,n}$. The ratio $Q_{0,p}/Q_{0,n}$ may therefore be examined as a stable observable of the band (considered further in Sec. IV B).

¹⁰ In considering the present enhancements, one should note that these comparisons are of *matrix elements*. Comparisons of nuclear transition data with Weisskopf estimates are often carried out for $B(E2)$ values, *i.e.*, proportional to *squared* matrix elements. Taking the present matrix elements in square would, of course, significantly amplify the quoted ratios of the calculated value to the single particle value.

¹¹ The gamma width must first be transformed to a $B(E2)$ value, which is then simply related to the intrinsic quadrupole moment by (6). However, the conversion involves a factor of E_γ^5 , where E_γ is the transition gamma-ray energy. Thus, the deduced $B(E2)$ and, hence, $eQ_{0,p}$ is highly sensitive to the energy taken for the 4^+ resonance. While we have used the evaluated energy [47] to deduce E_γ , Datar *et al.* [48] use the resonance parameters from alpha scattering, yielding a larger $B(E2)$ value, from which one obtains $eQ_{0,p} = 27.2(13) \text{ efm}^2$.

IV. BAND DISCUSSION

A. Rotational patterns

We are now in a position to examine the energies and electromagnetic observables, as laid out Sec. III, in the context of rotational structure and, in particular, to survey the patterns emerging in the rotational bands along the Be isotopic chain. We are interested not only in agreement of the calculated observables with a rotational picture but also in the nature of the deviations from rotational behavior. While some of these discrepancies may simply be numerical artifacts of incomplete convergence, as explored in Sec. IIID, others indicate physical deviations from the simplest picture of adiabatic rotation. Such deviations are to be expected from the various reasonable physical scenarios, *e.g.*, that the eigenfunctions reflect valence shell physics, or that they involve α clusters surrounded by weakly coupled neutrons. It is perhaps more remarkable, not that these deviations arise, but that they are not so large as to overwhelm the underlying rotational signatures.

Although rotational band structure is robustly apparent, persisting across calculations of varying basis sizes, the rotational patterns are being observed in incompletely converged values of observables. Many of the details — certainly many of the quantitative measures and also likely, to some extent, qualitative features of the bands — are therefore still in flux, *i.e.*, dependent upon the basis truncation parameter N_{max} and the oscillator length scale. Therefore, our interest in the following discussion principally resides in examining the qualitative properties of the rotational patterns which emerge from these *ab initio* calculations and recognizing the different varieties of band structure which are found, rather than in extracting definitive numerical predictions for comparison with experiment. Detailed quantitative comparisons with experimentally identified rotational bands in the Be isotopes will likely require the application of basis extrapolation methods [16, 37, 49, 50] to deduce the converged values for energies and electromagnetic observables.

Recall that candidate band members are identified based on both energies and electric quadrupole strengths (Sec. IIIB). The general pattern of agreement between the energies of these band members and the expected rotational values, for the different bands (Figs. 3 and 4), broadly falls into one of three qualitatively different categories:

- (1) The band terminates at (or below) the maximal angular momentum permitted within

the valence space (see Sec. III B), *i.e.*, no further candidate band members are identified beyond this angular momentum, and good agreement in energies is obtained for all band members. This category includes the ^9Be natural parity yrast and excited bands [Fig. 3(b)], ^{11}Be natural parity yrast band [Fig. 3(d)], ^{11}Be unnatural parity yrast band [Fig. 3(e)], and ^{10}Be yrast band [Fig. 4(b)]. The severely truncated yrast “band” of ^{12}Be [Fig. 4(c)] may also be associated with this category, to the extent that it can meaningfully be interpreted as a rotational band.

(2) Further candidate band members are identified above the maximal valence angular momentum, but, while good agreement in energies is obtained up to this angular momentum, the band members above this angular momentum deviate from rotational energies. In particular, the band members above the valence cutoff are found to lie high in energy relative to the rotational formula. This category includes the ^7Be natural parity yrast band [Fig. 3(a)], ^9Be unnatural parity yrast band [Fig. 3(c)], and ^8Be yrast band [Fig. 4(a)].

(3) Further candidate band members are identified above the maximal valence angular momentum, and good agreement in energies is obtained for all band members, persisting above the maximal valence angular momentum with no noticeable discontinuity. This category includes the ^{11}Be natural parity excited band [Fig. 3(d)], ^{10}Be excited band [Fig. 4(b)], and ^{12}Be excited band [Fig. 4(c)].

For bands in the second category, the discontinuity at the maximal valence angular momentum might not necessarily reflect a true difference in the *ab initio* description of the band members below this angular momentum and above it — as would be obtained in a fully converged calculation — but rather may, at least in part, reflect the difference in convergence rates of these levels, as already noted in Sec. III D. The discontinuity will clearly be modified as convergence continues with increasing N_{max} , and it could conceivably disappear for sufficiently large N_{max} . Therefore, the distinction between bands in the second and third categories is not necessarily rigid. Similarly, it is conceivable that some bands which, in the present analysis, are classified into the first category, *i.e.*, terminating at the maximal valence angular momentum, could develop further identifiable band members in more completely converged calculations, and therefore be reclassified into the second or third category.

For the $K = 1/2$ bands, as a result of the Coriolis contribution to the kinetic energy, alternate band members are raised into a region of higher density of states (Sec. III B).

This may result in fragmentation, as in the ^{11}Be unnatural parity yrast band at $J = 11/2$ [Fig. 3(e)], or in a disturbance in energy for a raised band member relative to the rotational expectation but without manifest mixing, as in the ^9Be unnatural parity yrast band at $J = 11/2$ [Fig. 3(c)]. On the other hand, comparatively close spacing in energies between levels ($< 1\text{ MeV}$) is also possible, without obvious fragmentation or perturbation arising, as at $J = 5/2$ for the ^7Be natural parity yrast band [Fig. 3(a)]. It must be realized that these specifics are of interest only as examples of what *can* happen in the calculation, not as necessarily robust predictions for fragmentation in these particular rotational bands. Due to the differences in convergence rates of different levels, chance proximities of the band members with background states may arise at specific N_{max} values. The disturbances to individual levels are therefore highly ephemeral features of the calculations, appearing and disappearing as N_{max} increases.

Further considering the energies within these $K = 1/2$ bands, recall that the expected rotational curves shown in Fig. 3 are based on a simple estimate of the rotational band energy parameters in (3), extracted from just the lowest three band members. This simple fit suffices to reproduce the energies of higher bands members to a remarkable degree, when compared, *e.g.*, to the energy spacings between successive levels within the band (tens of MeV) or to the changes in the calculated energies with each step in N_{max} due to incomplete convergence (several MeV). For instance, for the ^9Be natural parity excited $K = 1/2$ band [Fig. 3(b)], the NCCI calculation for the energy of the $J = 7/2$ band member matches the rotational estimate, based on the $J = 1/2$ through $5/2$ band member energies, to within $\sim 0.2\text{ MeV}$.

The ^9Be natural parity bands [Fig. 3(b)] merit special comment, among the candidate bands considered here, in that both natural parity bands are confined to the angular momenta permitted within the valence space. The excited band terminates at $J = 7/2$, while the yrast band extends to the maximal valence angular momentum, that is, $J = 9/2$. Although the terminating $J = 9/2$ band member is most closely identified with the yrast band, on the basis of quadrupole transitions, there is also significant $B(E2)$ strength from this state to the excited band members: mainly to the $J = 5/2$ member of the excited band (at ~ 0.4 times the in-band strength), but also somewhat to the $J = 7/2$ member (at ~ 0.1 times the in-band strength). In contrast, the second $J = 9/2$ state does not appear to be significantly connected to the excited band, despite being near the energy which would be

expected from the rotational formula for a $J = 9/2$ member of the excited band, instead primarily decaying to the remaining (second) low-lying $J = 7/2$ state.

The agreement between the calculated electric quadrupole matrix elements and the expected rotational values, as laid out in Figs. 5–15(a,b), while certainly not exact, nonetheless suggests a remarkably clean separation of rotational and intrinsic degrees of freedom in the *ab initio* NCCI calculations. This agreement is typically found to be best at lower angular momentum, deteriorating for higher angular momentum band members, but to an extent which varies greatly among the bands. Several patterns may be noted:

(1) For the bands in the first category above, *i.e.*, which terminate at (or below) the maximal valence angular momentum, there is a tendency for the quadrupole observables involving the terminating band member to exhibit larger deviations from the rotational expectations: consider the $J = 9/2$ band member of the ^9Be natural parity yrast band [Fig. 6 (top)], $J = 7/2$ band member of the ^{11}Be natural parity yrast band [Fig. 9 (top)], and $J = 4$ band member of the ^{10}Be natural parity yrast band [Fig. 13 (top)]. However, the quadrupole observables do not exhibit noticeable termination effects at $J = 7/2$ in the ^9Be natural parity excited band [Fig. 7 (top)]. It is worth noting that termination effects are to be expected in the Elliott $\text{SU}(3)$ shell model description of nuclear rotation, in which quadrupole strengths within a band decline as band termination is approached (see discussion in Ref. [7]). A similar fall-off can be obtained in $\text{Sp}(3, \mathbb{R})$ symplectic calculations [51] of rotational bands (see Fig. 6 of Ref. [52]). However, it is difficult to isolate signs of such systematic mechanisms for band termination phenomena from the possible confounding effects of mixing, since the yrast states also become less well isolated in energy at these higher angular momenta.

(2) For the bands in the second and third categories above, *i.e.*, which extend beyond their corresponding maximal valence angular momenta, there may (or may not) be a discontinuity in the quadrupole observables at the maximal valence angular momentum. This behavior is somewhat, but not entirely, correlated with that of the energies. Recall that there is a discontinuity in energies in the ^7Be natural parity yrast band [Fig. 3(a)], ^9Be unnatural parity yrast band [Fig. 3(c)], and ^8Be natural parity yrast band [Fig. 4(a)] at the maximal valence angular momentum. There is a corresponding discontinuity in the quadrupole *moments* for these bands in ^7Be [Fig. 5(a)], possibly ^9Be [Fig. 8(a)], and ^8Be [Fig. 12(a)]. However, there is no apparent discontinuity in the quadrupole *transition matrix elements* in ^7Be [Fig. 5(b)] and ^9Be [Fig. 8(b)]. For ^8Be [Fig. 12(b)], a significant deviation arises only at $J = 8$,

by which point the band has moved off the yrast line, although a change in curvature might putatively already be evident at $J = 6$. The deviations of the calculated quadrupole moments and transition matrix elements, for the band members above the maximal valence angular momentum, are uniformly toward larger magnitudes relative to the rotational values. For the bands in the third category above, *i.e.*, for which the energies continue to follow the rotational expectation past the maximal valence angular momentum — namely, the ^{11}Be natural parity excited band [Fig. 3(d)], ^{10}Be natural parity excited band [Fig. 4(b)], and ^{12}Be natural parity excited band [Fig. 4(c)] — the quadrupole moments and transition matrix elements are similarly consistent with the expected rotational values (Figs. 10, 14, and 15, respectively), with the exception that reduced strengths are found for the highest identified band member, at $J = 8$, in ^{12}Be .

(3) Not unexpectedly, states in regions of higher level density are susceptible to fragmentation (or mixing) effects, which are reflected in the quadrupole moments of those states and in transitions involving those states, as either the initial or final state. For instance, for the unnatural parity yrast band of ^{11}Be [Fig. 11 (top)], note that it is the band members which have been raised in energy by the Coriolis staggering — with $J = 7/2$ and $11/2$ [Fig. 3(e)] — for which the values for the quadrupole moments and transition matrix elements deviate from the rotational values (or, rather, for the $J = 11/2$ band member, significant fragmentation over two states precludes unambiguous comparison).

For the $K = 0$ bands, in the even-mass isotopes, it is natural to consider the calculated $E(4^+)/E(2^+)$ energy ratios (*e.g.*, Ref. [53]). Specifically, we must restrict our attention to the yrast bands, in ^8Be and ^{10}Be , due to fragmentation of the $J = 2$ state in the excited band. The expected rotational ratio is $E(4^+)/E(2^+) = 10/3 \approx 3.33$. For both ^8Be and ^{10}Be , the energy ratios are somewhat higher, at 3.41 and 3.50, respectively. The experimental values [47] similarly lie above the rotational ratio, at 3.75(5) and 3.49, respectively.¹²

Similarly, for these bands, it is natural to compare the quadrupole moment of the $J = 2$ state and the $2 \rightarrow 0$ transition matrix element, or, customarily, the $B(E2; 2 \rightarrow 0)$ reduced transition probability, against a rotational description. This is essentially the comparison already being made by comparison of the data point at $J = 2$ with the rotational curve in

¹² The $E(4^+)/E(2^+)$ ratio indicated for ^{10}Be is based on a tentative spin-parity assignment of 4^+ for the 11.7 MeV level [47].

the plots of the ^8Be yrast band [Fig. 12(b)] and ^{10}Be yrast band [Fig. 13(b)] transition matrix elements. The normalization of the curve indicating rotational values is, for these bands, determined from $Q(2)$, so the proximity of the calculated data points to the rotational curve indicates agreement between $Q(2)$ and $B(E2; 2 \rightarrow 0)$. Specifically, Q_0 is obtained from $Q(2)$ via the rotational relation $Q(2)/Q_0 = -2/7$, and the rotational expectation for the transition strength is in turn given in terms of this Q_0 by $B(E2; 2 \rightarrow 0)/(eQ_0)^2 = 1/(16\pi) \approx 1.99 \times 10^{-2}$. In the present calculations, the yrast band of ^8Be [Fig. 12(b)] has $B(E2; 2 \rightarrow 0)/(eQ_0)^2 = 1.96 \times 10^{-2}$, in agreement with the rotational value to within $\sim 1.3\%$.¹³ The yrast band of ^{10}Be [Fig. 13(b)] has $B(E2; 2 \rightarrow 0)/(eQ_0)^2 = 2.10 \times 10^{-2}$ for the proton quadrupole operator, in agreement with the rotational value to within $\sim 6\%$, but 3.13×10^{-2} for the neutron quadrupole operator, deviating more substantially (as already apparent from Fig. 13). However, even the severely truncated yrast band in ^{12}Be yields ratios $B(E2; 2 \rightarrow 0)/(eQ_0)^2 = 3.7 \times 10^{-2}$ for the proton quadrupole operator and 3.2×10^{-2} for the neutron quadrupole operator, still within a factor of two of the rotational values. For the excited $K = 0$ bands in ^{10}Be and ^{12}Be , recall that is used instead of $Q(2)$ for normalization, due to fragmentation of the $J = 2$ band member, and the same comparison cannot directly be made.

The magnetic dipole moments and transition matrix elements bring a physically complementary set of observables to the problem of identifying rotational structure in these bands, with more robust convergence properties than the quadrupole observables (Sec. III D). For the odd-mass isotopes, the analysis of the dipole observables is more complicated than for the quadrupole observables, due to the greater number of relevant parameters (as discussed in Sec. III C). However, the dipole observables are the most cleanly rotational, even at high angular momenta. Recall that the curves indicating the expected rotational values for these observables, shown at bottom in Figs. 5–15, are based on a simultaneous fit to moments and transition matrix elements, generally restricted to the lower angular momentum band members.

For the odd-mass isotopes, let us consider the behavior of the magnetic dipole observables under the three different band termination scenarios. In the bands in the first category,

¹³ Note that considering the square of the transition matrix element, to obtain the $B(E2)$ strength, approximately doubles the relative deviation between the calculated and rotational values — *e.g.*, for ^8Be the agreement of the transition matrix element itself with the rotational value is at the $\sim 0.6\%$ level.

with termination at (or below) the maximal valence angular momenta, deviations from the expected rotational values arise in roughly the same terminating states as for the electric quadrupole matrix elements. There are modest deviations at the terminating $J = 9/2$ state in the ^9Be natural parity yrast band [Fig. 6(c,d)], but not for the terminating $J = 7/2$ state of the excited band [Fig. 7(c,d)], consistent with the pattern for the quadrupole observables. Similarly, deviations occur at the $J = 7/2$ termination for the ^{11}Be natural parity yrast band [Fig. 9(c,d)], and fragmentation again obscures the situation for the ^{11}Be unnatural parity yrast band [Fig. 11(c,d)]. For the remaining bands, in the second and third categories, *i.e.*, which continue through the maximal valence angular momentum, the calculated dipole term moments and transition matrix elements are consistent with rotational values to the highest angular momentum considered. This agreement holds regardless of the deviations found earlier for quadrupole moments or transition matrix elements (Figs. 5, 8, and 9).

B. Observables reflecting intrinsic structure

So far we have focused on the *existence* of rotational structure rather than the *intrinsic structure* underlying this rotation. That is, we have been concerned with the extent to which the observable patterns are consistent with an adiabatic separation of the wave function as in (1), into rotational and intrinsic factors, rather than exploring the nature of the intrinsic state itself. Nonetheless, some of the observables we are considering do have the potential to shed light on the intrinsic state.

Although the intrinsic quadrupole moment itself, taken on an absolute scale, is an obvious choice for an intrinsic structural indicator, as a measure of deformation, it is rendered largely uninformative by its incomplete convergence (Sec. III D). In contrast, as noted in Sec. III D, the ratio $Q_{0,p}/Q_{0,n}$ (Fig. 18) appears to be relatively converged and thus provides a stable measure comparing the proton and neutron structure within the intrinsic state. For instance, in Fig. 18, consider the behavior of $Q_{0,p}$ and $Q_{0,n}$ as functions of N_{max} for the natural parity yrast and excited bands of ^9Be . As noted earlier, these two bands both terminate at angular momenta consistent with valence space structure. From Fig. 18, it is apparent that these bands have both $Q_{0,p}$ values which closely track each other as the basis N_{max} increases, and similarly for $Q_{0,n}$ values, resulting also in closely matching ratios $Q_{0,p}/Q_{0,n}$. This is consistent with — though hardly a conclusive indicator of — related underlying intrinsic

structures for these two bands, at least as far as quadrupole correlations are concerned.

More generally, there is a clear separation of the bands into two clusters in the $(Q_{0,p}, Q_{0,n})$ space of Fig. 18. The natural parity yrast bands (plus the ^9Be natural parity excited band) all have ratios $Q_{0,p}/Q_{0,n} \gtrsim 1$, *i.e.*, lying just above the diagonal dashed line in Fig. 18. (These bands all fall into either the first or second categories, according to band termination.) The remaining natural parity excited bands and the unnatural parity bands (which fall into the second and third categories) are instead clustered well below (or, equivalently, to the right of) the diagonal dashed line. For each of these bands, $Q_{0,n}$ is about twice $Q_{0,p}$. Incomplete convergence makes it unreliable to compare $Q_{0,p}$ and $Q_{0,n}$ values directly across different bands in Fig. 18, since the quadrupole observables for these different bands may exhibit different convergence rates. Nonetheless, comparison of bands within the same nucleus, in calculations at the same N_{max} , are suggestive. They indicate that change in the ratio of $Q_{0,p}$ and $Q_{0,n}$ between the two clusters of bands arises primarily from an approximate doubling in $Q_{0,n}$, rather than from any significant change in $Q_{0,p}$.

It is interesting to consider the present results for $Q_{0,p}$ and $Q_{0,n}$ in light of the results of antisymmetrized molecular dynamics (AMD) calculations, in particular, for ^{10}Be , from Ref. [54]. In the AMD framework, a cluster structure arises consisting of an $\alpha + \alpha$ dimer plus two “valence” neutrons. In the yrast band, the two valence neutrons are predominantly in π orbitals, extending perpendicular to the symmetry axis of the $\alpha + \alpha$ dimer. In the excited band, the two valence neutrons are predominantly in σ orbitals. These latter orbitals extend along the symmetry axis, giving rise to a more pronouncedly prolate mass distribution. Such a change in neutron distribution between bands is at least qualitatively consistent with the increased neutron intrinsic quadrupole moment for the excited band in the present calculations. It also provides an explanation for the lower rotational constant (higher moment of inertia) of the excited band, as arising from a more prolate mass distribution induced by the valence neutrons. The AMD calculations also indicate that the yrast π -orbital states are largely p -shell in character, while the σ -orbital states display enhanced clustering and draw heavily on $2\hbar\Omega$ and higher excitations in a shell-model picture. This proposed difference in structure is consistent with the differing termination behaviors identified for the ^{10}Be yrast and excited bands in the present calculations.

The magnetic dipole observables likewise are capable of providing insight into the underlying structure, through comparison of the strengths of the different dipole terms. (The

dipole strengths taken individually, on an absolute scale, could also yield insight through comparisons with appropriate models of the intrinsic structure.) In particular, the dipole observables obtained with the different dipole term operators $\mathbf{D}_{\ell,p}$, $\mathbf{D}_{\ell,n}$, $\mathbf{D}_{s,p}$, and $\mathbf{D}_{s,n}$ allow the proton and neutron, as well as orbital and spin, contributions to the angular momentum structure of the band members to be probed independently.

Let us therefore examine the moments and transition matrix elements arising from the individual dipole terms in greater detail, beginning with the odd-mass isotopes. Recall that, in a rotational interpretation, the moments [Figs. 5–11(c)] receive contributions from the core rotor — yielding a term linear in J — as well as intrinsic matrix elements (the direct and cross terms), while only these latter contribute to the transition matrix elements [Figs. 5–11(d)]. The numerical values of the a_0 , a_1 , and, for $K = 1/2$ bands, a_2 coefficients extracted from the rotational fits for the odd-mass isotopes are summarized in Table II.

The dipole terms yielding the largest moments are generally the proton and neutron orbital operators $\mathbf{D}_{\ell,p}$ and $\mathbf{D}_{\ell,n}$, as evident both from the values of the individual moments in the plots and the magnitudes of the overall fit coefficients in Table II. The moments from the orbital operators are generally linearly increasing in J , suggesting that the moments primarily arise from a core rotor contribution [see Fig. 2(a)]. Note that the core rotor term rapidly outstrips the intrinsic terms, with increasing J , if the values of a_0 and of the intrinsic coefficients a_1 or a_2 are comparable in magnitude. A substantial but subordinate contribution from the intrinsic direct term appears as a modification of the slope of the moment curve at low J , together with a displacement of the intercept to a nonzero value when the curve is extrapolated to $J = 0$.¹⁴ A contribution from the intrinsic cross term appears as staggering in the moment curve.

Let us take the ^9Be natural parity bands (Figs. 6 and 7) for illustration. As a starting point for interpretation, it is helpful to keep in mind the model of ^9Be as an $\alpha + \alpha$ dimer, which may be taken as the core rotor, plus an additional neutron, which may be taken as the extra-core particle. Recall that the coefficient a_0 describing the contribution of the core rotor term represents the effective gyromagnetic ratio of the core, that is, except for inclusion of the dimensionful factor μ_N (Sec. II D). The core rotor contributions for protons are nearly

¹⁴ However, care must be taken in attempting to identify such a displacement simply from inspection of the figures. A nonzero intercept is especially hard to identify for the $K = 3/2$ bands, since the J axes of the plots start at $J \approx K$, not at the origin. The coefficients in Table II should be relied upon instead.

the same, at $a_0 \approx 0.54 \mu_N$ and $0.56 \mu_N$, for the ground and excited bands, respectively (see Table II), differing by only $\sim 3\%$. The core rotor for ${}^9\text{Be}$ need not be identical to that of ${}^8\text{Be}$, due to possible modifications of the $\alpha + \alpha$ dimer by the presence of the additional neutron. However, these ${}^9\text{Be}$ results are loosely consistent with the value $a_0 \approx 0.49 \mu_N$ obtained for the yrast band of ${}^8\text{Be}$. The core rotor gyromagnetic ratios for the neutrons show greater variation between the two bands, at $a_0 \approx 0.36 \mu_N$ and $0.44 \mu_N$, respectively, perhaps indicating that, contrary to the simplest interpretation, the last neutron does modify or contribute to the “core” neutron structure. Note that these results lie below the ${}^8\text{Be}$ value. It would be reasonable, in the picture where the core rotor is the $\alpha + \alpha$ dimer, and under the basic assumption that only the extra-core particles should contribute to the intrinsic matrix elements [1], to expect the proton orbital observables to result entirely from the core gyromagnetic contribution, with no intrinsic contribution, while the neutron orbital observables would have an intrinsic contribution from the extra-core neutron. However, from the a_1 and a_2 coefficients in Table II, it is apparent that both the proton and neutron orbital operators yield sizeable intrinsic matrix elements, *e.g.*, for the ground state band, the values are $a_1 \approx -0.86 \mu_N$ for the protons and $+0.48 \mu_N$ for the neutrons, so the intrinsic matrix element for the proton operator is actually larger in magnitude than that for the neutron operator, though, incidentally, of opposite sign.

Considering the spin dipole terms, if the protons are all confined to α particles, their spins should be pairwise coupled to zero, and we would expect vanishing spin dipole matrix elements for the protons. The $\mathbf{D}_{s,p}$ observables in these bands are indeed essentially vanishing, compared to the other magnetic dipole observables, as apparent from Figs. 6 and 7 (or Table II). For the neutron spin operator, the extra-core neutron can contribute. The neutron spin dipole observables are dominated by the intrinsic contribution (specifically, the direct term, even for the excited band, where the cross term could contribute), with negligible core contribution.

Indeed, across the Be isotopes, the dipole moments and transition matrix elements for the proton spin operator $\mathbf{D}_{s,p}$ are consistently suppressed, as evident both from the comparatively small values of the individual moments in the plots and from the coefficients in Table II, all $\lesssim 0.1 \mu_N$. The largest values arise in the ${}^{11}\text{Be}$ yrast band terminating state [Fig. 9(c)], for which sizeable deviations from rotational expectations for the calculated electromagnetic observables have already been noted. The intrinsic matrix element con-

tributions, for the various dipole term operators, may be more cleanly examined in the calculations for transition matrix elements [Figs. 5–11(d)], where they are not obscured by the core rotor contribution. The neutron spin operator $\mathbf{D}_{s,n}$ never generates a sizeable core rotor contribution (a_0 coefficient) but does give rise to substantial intrinsic matrix elements, comparable to those obtained for the orbital dipole operators. The only dipole term with consistently negligible intrinsic matrix elements is the proton spin term, as already noted. The intrinsic matrix elements for the remaining dipole terms — proton orbital, neutron orbital, and neutron spin — variously take on greater or lesser strengths for the different bands under consideration.

For the even-mass isotopes [Figs. 12–15(c)], in a rotational picture, the dipole moments arise exclusively from the core rotor contribution. The calculated moments do indeed generally follow the expected linear behavior with respect to J . The exception is the ^{10}Be natural parity yrast band [Fig. 13(c)], for which the moments of the $J = 2$ and 4 states do not follow a simple linear relation. However, the quadrupole observables also deviated markedly from rotational relations for these states. For the bands which continue past the maximal valence angular momentum — namely, the ^8Be natural parity yrast band [Fig. 12(c)], the ^{10}Be natural parity excited band [Fig. 14(c)], and the ^{12}Be natural parity excited band [Fig. 15(c)] — the dipole moments closely follow the expected linear dependence on J (aside from fragmentation at $J = 2$ in ^{10}Be). Note that there is no discontinuity at the maximal valence angular momentum. The spin dipole terms are negligible compared to the orbital dipole terms, consistent with the small core rotor contributions found for these terms in the bands of the odd-mass isotopes.

We may finally compare gyromagnetic ratios for the proton and neutron orbital dipole operators in these $K = 0$ bands of the even-mass isotopes. They are strictly identical in ^8Be [Fig. 12(c)], by isospin symmetry. For the two remaining natural parity yrast bands, meaningful comparison is difficult: recall the deviation from rotational behavior in the yrast band of ^{10}Be [Fig. 13(c)] and the severely truncated nature of the yrast “band” in ^{12}Be , for which we can only consider the dipole moments for the $J = 2$ state (only the moment for the proton orbital dipole term is substantial, at $\sim 1.5 \mu_N$, while those for all other dipole terms are $\lesssim 0.3 \mu_N$). In the ^{10}Be [Fig. 14(c)] and ^{12}Be [Fig. 15(c)] excited bands, the moments for the neutron orbital dipole term are more than twice those for the proton orbital dipole term, ostensibly reflecting the neutron excess in these nuclei. Recall that the individual

dipole terms ($\mathbf{D}_{\ell,p}$, $\mathbf{D}_{\ell,n}$, $\mathbf{D}_{s,p}$, and $\mathbf{D}_{s,n}$) are proportional to the different angular momentum operators (ℓ_p , ℓ_n , s_p , and s_n) which together add up to the total angular momentum operator. Consequently, the dipole moments calculated for these different dipole terms are proportional to the contribution of the corresponding angular momentum operator to the total angular momentum.¹⁵ Thus, *e.g.*, for the ^{12}Be excited band, the values $a_0 \approx +0.27 \mu_N$, $+0.66 \mu_N$, $+0.012 \mu_N$, and $+0.07 \mu_N$, obtained for these dipole terms, respectively, indicate that the angular momenta of the band members all receive approximately proportionate contributions, of $\sim 27\%$ from proton orbital motion, $\sim 66\%$ from neutron orbital motion, $\sim 1\%$ from proton spin, and $\sim 7\%$ from neutron spin.

C. Rotational energy parameters

Let us finally now focus on the global properties of the rotational spectra, namely, the band energy parameters. Our purpose is both to explore what these parameters may indicate about the structure of the calculated bands and to obtain points of comparison to the experimental data for proposed rotational bands in the Be isotopes.

Recall that the parameters appearing in the rotational energy relations (2) and (3) are the band energy E_0 , the rotational constant A , and, for $K = 1/2$ bands, the Coriolis decoupling parameter a . In a plot of energies *vs.* $J(J+1)$ (as in Figs. 3 and 4), these parameters represent the “height” or energy intercept of the band, the “slope” of the band, and the “staggering” of the band, respectively. The values of these parameters, as extracted from fits of the rotational energy relation to the energies of the calculated band members (as described in Sec. III B), are shown in Fig. 19, with the odd-mass isotopes at left and even-mass isotopes at right. The band energy [Fig. 19(d,e)] is presented as a band *excitation* energy E_x , obtained by taking the band energy E_0 extracted for the given band relative to the energy E_0 similarly extracted for the natural parity yrast band. Results obtained from calculations with successive values of N_{\max} ($N_{\max} = 6, 8$, and 10 for natural parity bands,

¹⁵ In general, if a total angular momentum operator is obtained as a sum of components $\mathbf{J} = \sum_i \mathbf{J}_i$, then the fractional contribution of any particular component operator \mathbf{J}_i to the total angular momentum of a state $|\psi_J\rangle$ is given by $f_i \equiv \langle \mathbf{J}_i \cdot \mathbf{J} \rangle / \langle \mathbf{J} \cdot \mathbf{J} \rangle = [J(J+1)(2J+1)]^{-1/2} \langle \psi_J | \mathbf{J}_i | \psi_J \rangle$. This latter reduced matrix element $\langle \psi_J | \mathbf{J}_i | \psi_J \rangle$ also defines the dipole moment calculated taking \mathbf{J}_i as the dipole operator, to within geometrical factors involving J . Note that the angular momentum fractions f_i necessarily sum to unity, by the definition of \mathbf{J} as the sum of the \mathbf{J}_i .

or $N_{\max} = 7, 9$, and 11 for unnatural parity bands) are represented by symbols of increasing size. Note that the band parameters at the highest N_{\max} are determined by the same energy fits as shown in Figs. 3 and 4.

Ideally, comparison of the calculated and experimental band parameters provides a direct test of the degree to which the nuclear many-body problem with the chosen internucleon interaction (here, JISP16) reproduces the rotational dynamics actually occurring in the physical Be isotopes. However, this comparison is subject to limitations from both calculational and experimental considerations.

From the calculational side, we must consider the extent to which the values for band parameters obtained from the present truncated calculations are converged. The N_{\max} dependence of the relative energies of calculated band members was already explored in ${}^9\text{Be}$ (Sec. III D), providing some insight into what type of evolution with N_{\max} may be expected. The dependence of the parameter values on N_{\max} shown in Fig. 19 more directly provides an indication of the robustness of these results with respect to the N_{\max} truncation (as discussed in further detail for each of the parameters below).

From the experimental side, clear-cut identification of rotational band members in the Be isotopes is challenging, since prospective band members may include wide or poorly-resolved resonances, spin-parity assignments are missing or uncertain for many of the known states, and electromagnetic transition data are largely unavailable [42, 46, 47], although reaction amplitudes or decay widths (*e.g.*, Refs. [55–57]) can provide structural indicators relevant to band identification. Experimental candidates for rotational bands in the Be isotopes ($8 \leq A \leq 12$) are surveyed by Bohlen *et al.* [58]. Only two or three low-lying band members need be identified in order to extract an estimate of the band parameters. However, the parameter values obtained for the experimental bands are, naturally, sensitive to the choice of included band members and the energies adopted for these. Values obtained from fits to the experimentally observed bands are shown in Fig. 19 (indicated by horizontal lines). In generating these fits, we have used the band members and energies indicated in Table III.

The values for the rotational parameter A extracted from the calculations [Fig. 19(a,b)] appear to be sufficiently stable with respect to N_{\max} to warrant at least a qualitative analysis for all the bands. Recall the convergence pattern observed for the band members of ${}^9\text{Be}$ in Fig. 16. Although the energies of the band members shift by several MeV with increasing N_{\max} , the relative energies within the band, which determine the slope A , remain compar-

actively unchanged. The largest N_{\max} dependence of A is found for the ^8Be , ^9Be , and ^{10}Be natural parity yrast bands. However, each successive step in N_{\max} brings a change which is smaller by a factor of at least 1.5, suggesting a reasonably rapid approach to a converged value.

The value of the rotational parameter varies by a factor of ~ 2 across the different calculated bands. Indeed, this variation is apparent by inspection of Figs. 3 and 4, from the range of slopes of the energy fit lines. We may observe that the variation in A across the bands follows a trend which correlates with the clustering of bands according to $Q_{0,p}/Q_{0,n}$ ratios (see Fig. 18) discussed in Sec. IV B, into bands with approximately equal proton and neutron quadrupole moments ($Q_{0,p}/Q_{0,n} \gtrsim 1$) and those with an enhanced neutron quadrupole moment ($Q_{0,p}/Q_{0,n} \sim 0.5$). From Fig. 19(a,b), the former bands are seen to be the “steep” bands ($A \gtrsim 0.5$ MeV), while the latter bands are seen to be the “shallow” bands ($A \lesssim 0.5$ MeV). The distinction is particularly clear if one compares the yrast and excited bands *within* a single isotope in Fig. 19(a,b). Although the connection between quadrupole deformation (measured by Q_0) and rotational moment of inertia (hence, A) is only uniquely defined if model assumptions about the nature of the rotational motion are imposed (*e.g.*, Refs. [3, 5]), the observed correlation between $Q_{0,p}/Q_{0,n}$ and A is reasonable from simple arguments. If the enhanced neutron quadrupole moment represents a greater extension of the neutron distribution along the symmetry axis (*e.g.*, due to neutrons in σ orbitals) as interpreted in Sec. IV B, this may be expected to lead to a greater moment of inertia for rigid rotation, and thus a reduced rotational energy scale A (Sec. II B).

A wide range in values for the rotational parameter A is also found experimentally in the Be isotopes, as surveyed by Bohlen *et al.* [58]. Comparing the parameter values for the calculated and experimental bands, and excluding the bands in ^{12}Be from this discussion (to be considered further below), we observe that the values for A extracted from the highest N_{\max} calculation lie within ~ 0.1 MeV of the experimental values. Qualitatively, the pattern of which bands fall into the “steep” *vs.* “shallow” is consistent between the calculations and experiment. With increasing N_{\max} , the A parameters for the calculated bands (still excepting ^{12}Be) are decreasing. Except in the case of the ^9Be natural parity excited band, this brings the calculated values further toward the experimental values.

The Coriolis staggering for the calculated $K = 1/2$ bands, measured by the decoupling parameter a [Fig. 19(c)], varies both in amplitude and sign. The values obtained for a are

sufficiently stable with respect to N_{\max} to permit an examination of the trends in its value across the bands. The energy staggering in the calculated ${}^7\text{Be}$ natural parity yrast band [Fig. 3(a)] is such that the $J = 1/2, 5/2, \dots$ levels are raised in energy, and the $J = 3/2, 7/2, \dots$ levels are lowered. This corresponds to a negative value of the decoupling parameter ($a \approx -1.4$ at $N_{\max} = 10$). Note that the staggering is sufficiently pronounced that the two lowest- J band members are inverted, as is experimentally observed for this nucleus [46]. Positive values of the decoupling parameter are obtained for all other candidate $K = 1/2$ bands. Of these, the natural parity bands (namely, in ${}^9\text{Be}$ [Fig. 3(b)] and ${}^{11}\text{Be}$ [Fig. 3(d)]) exhibit lesser staggering ($a \lesssim 1$), while the unnatural parity bands (namely, in ${}^9\text{Be}$ [Fig. 3(c)] and ${}^{11}\text{Be}$ [Fig. 3(e)]) exhibit more marked staggering ($a \approx 2$). This categorization of the bands by sign and magnitude of staggering is consistent with the experimentally observed pattern.¹⁶ Furthermore, with increasing N_{\max} , the calculated values are all decreasing in magnitude, which serves to bring them closer to the experimental values.

The excitation energies E_x for the calculated bands [Fig. 19(d,e)] vary considerably in their rates of convergence. For instance, the excitation energy of the unnatural parity band in ${}^{11}\text{Be}$ decreases by less than 0.1 MeV, as N_{\max} increases from 7 to 11, while that of the natural parity excited band in ${}^{10}\text{Be}$ decreases by ~ 9 MeV, as N_{\max} increases over a comparable range, from 6 to 10. However, the rate of convergence of E_x follows a pattern consistent with the classification of the bands by the nature of their termination in Sec. IV A. In particular, the bands which either terminate or depart from the rotational energy formula at the maximal valence angular momentum (*i.e.*, bands in either of the first two categories defined in Sec. IV A) have excitation energies which exhibit the least dependence on N_{\max} — specifically, these are the ${}^9\text{Be}$ natural parity excited band, ${}^9\text{Be}$ unnatural parity band, and ${}^{11}\text{Be}$ unnatural parity band. These may be thought of as bands which, at least to some extent, respect the p -shell closure. Note that all excitation energies are being taken with respect to the natural parity yrast band, which likewise falls into one of the first two categories, so the convergence of these excitation energies serves to compare the convergence of two bands with ostensibly *similar* shell structures. In contrast, bands which exhibit no discontinuity in

¹⁶ See also the discussion in Ref. [31] for a comparison to the Coriolis staggering expected from the Nilsson model [59, 60], *i.e.*, based on a single unpaired particle in an axially-symmetric deformed mean field. A more detailed and realistic mean-field analysis might be carried out by estimating the signature splitting from a cranked Nilsson model [61].

energies at the maximal valence angular momentum (*i.e.*, bands in the third category) have excitation energies with the largest N_{\max} dependence — specifically these are the remaining natural parity excited bands, in ^{10}Be , ^{11}Be , and ^{12}Be .

In comparing the excitation energies with experiment, let us first consider the bands with the smaller N_{\max} dependence, for which a more concrete comparison can be made. The near degeneracy of the natural and unnatural parity yrast bands in ^{11}Be is qualitatively reproduced. Quantitatively, the experimental excitation energy of the unnatural parity band is $\sim 0.22\text{ MeV}$,¹⁷ while the excitation energy for this band from the *ab initio* calculations appears to be robustly $\sim 1.9\text{ MeV}$. In ^9Be , the calculated natural parity excited band and unnatural parity band lie within $\sim 1.2\text{ MeV}$ of each other, at the highest N_{\max} considered, approximately reproducing the near degeneracy found in experiment. These calculated energies are $\sim 3\text{--}4\text{ MeV}$ above the experimental values, but are descending toward the experimental values with increasing N_{\max} .

Moving on to the bands with larger N_{\max} dependence, the calculated excitation energies still lie $\sim 4\text{--}10\text{ MeV}$ above the experimental excitation energies, at the highest N_{\max} considered, but are rapidly falling with N_{\max} . It is therefore difficult to make a concrete comparison. For ^{12}Be , in particular, the excitation energy of the calculated excited band is nearly halved — from $\sim 11\text{ MeV}$ to $\sim 6\text{ MeV}$ — as N_{\max} increases from 6 to 10. It is therefore reasonable to expect the calculated excited band to fall to near degeneracy with the calculated ground state band. The experimental excited band in ^{12}Be is likewise low-lying, at $\sim 2.2\text{ MeV}$.¹⁸ Strong mixing may therefore be expected — both for the calculated and experimental bands — which could significantly affect the extracted values for the band parameters. Recall that the calculated yrast band for ^{12}Be [Fig. 4(c)] is radically truncated, terminating at the maximal p -shell valence angular momentum $J = 2$. Although experimental candidate states for 4^+ and even 6^+ members of both the yrast band [64, 65] and

¹⁷ Although the experimental $1/2^+$ *ground state* of ^{11}Be has *unnatural parity* [42], a situation described as “parity inversion” (Sec. III A), the *lowest energy band* (as defined by comparing E_0 parameters) is actually the *natural parity* $K^P = 1/2^-$ yrast band. The perhaps counterintuitive distinction between “ground state band” and “lowest energy band” arises from the difference in staggering between the bands: the larger staggering of the unnatural parity band depresses the energy of the $1/2^+$ band head state below that of the $1/2^-$ band head state, despite the higher overall band energy.

¹⁸ More highly-excited 0^+ bands in ^{12}Be , with $E_0 \approx 6.4\text{ MeV}$ [62] and $E_0 \approx 10.8\text{ MeV}$ [63], have also been reported.

excited band [66] have been proposed (see Ref. [58]), these identifications are not based on firm spin-parity assignments and therefore do not provide definitive grounds for comparison. In the shell model framework, the ground state and excited 0^+ states in ^{12}Be have been interpreted as being mixtures of $0\hbar\Omega$ closed p -shell configurations and $2\hbar\Omega$ configurations involving promotion of two neutrons to sd -shell orbitals (*e.g.*, Ref. [64, 67]). At least schematically, such shell model configurations may be associated with the p -shell terminating and non-terminating bands in the present calculations. Experimental results from, *e.g.*, knockout [68, 69], transfer [70], and charge exchange [71] reactions have been interpreted as suggesting significant mixing of these $0\hbar\Omega$ and $2\hbar\Omega$ configurations in both the ground and excited 0^+ states.

V. CONCLUSION

The emergence of rotational patterns is observed in *ab initio* NCCI calculation with realistic interactions, despite the principal challenge in identifying collective structure in NCCI calculations — namely, the weak convergence of many of the relevant observables. Eigenvalues and other calculated observables are dependent upon both the truncation N_{max} and the oscillator length parameter (or $\hbar\Omega$) for the NCCI basis. Although it may be possible to extrapolate the values of calculated observables to their values in the full, infinite-dimensional space [16, 49, 50], such methods are still in their formative stages and have not been developed for the crucial electric quadrupole observables. It is therefore particularly notable that quantitatively well-developed and robust signatures of rotation may be observed in the present results. That this is possible reflects the distinction between convergence of *individual* observables, taken singly, and convergence of *relative* properties, such as ratios of excitation energies or ratios of quadrupole matrix elements. It is these latter relative properties which are essential to identifying rotational dynamics and which are found to be sufficiently converged to yield stable rotational patterns at currently achievable N_{max} truncations — along with the well-converged magnetic dipole observables.

We find that rotational structure is pervasive in the NCCI calculations of the yrast and near-yrast regions of the p -shell Be isotopes. (Comparable results for ^{12}C are reported in Ref. [72].) With suitable basis extrapolation methods, we may hope to determine the extent to which *ab initio* calculations can provide quantitatively precise predictions of rotational

band properties (*e.g.*, the rotational formula energy parameters, including Coriolis decoupling). Even the present calculations, unconverged and unextrapolated, suggest a notable degree of qualitative consistency with the experimentally observed bands (Fig. 19).

While the emergence of rotation appears to be robust across different *ab initio* interactions [73], it remains to be seen in what ways the quantitative details of the rotation may be sensitive to the interaction. More broadly, different *ab initio* computational approaches can more or less readily access different correlations within the nuclear wave functions. Therefore, it is of particular interest to examine the emergence of rotation in approaches other than the NCCI framework. For instance, taking ${}^7\text{Be}$ (or its mirror nucleus ${}^7\text{Li}$) as an example, quantum Monte Carlo calculations readily reproduce the $3/2-1/2-7/2-5/2$ yrast angular momentum sequence [9], reflective of a $K = 1/2$ band with strong negative Coriolis staggering. Electromagnetic observables of the type considered in the rotational analysis can also readily be calculated by such methods for this nucleus [74].

Although the presence of rotational patterns suggests the separation of the wave function into rotational and intrinsic factors, it leaves open the question of the underlying structure of the intrinsic state, as noted in Sec. IV. Hints to this intrinsic structure may be obtained from the intrinsic observables (Sec. IV B), as well as the rotational parameters of the bands (Sec. IV C). For the Be isotopes, we may seek to determine the extent to which aspects of the rotational structure may be understood within different physical frameworks, including cluster structure (*e.g.*, $\alpha + \alpha$, $\alpha + n + \alpha$, *etc.*), Nilsson-like single-particle motion in a mean field, and valence shell structure (as suggested by the termination effects). Elliott $\text{SU}(3)$ symmetry [6, 7] provides the classic theoretical explanation of the emergence of rotation within the valence shell, while $\text{Sp}(3, \mathbb{R})$ symmetry [52] provides a natural context for the emergence of collective deformation and rotational degrees of freedom in the full multi-shell configuration space.

One may observe that the present discussion represents a phenomenological rotational analysis, in the traditional experimental sense, but of a large set of observables taken from calculations of the *ab initio* nuclear many-body problem. Having full access to the calculated wave functions permits analysis of an extended set of rotational observables, many of which are difficult or impossible to access experimentally. For example, we have presented results independently probing proton and neutron degrees of freedom, and orbital and spin degrees of freedom, through multipole operators involving the corresponding contributions

individually.

Furthermore, having direct access to the calculated wave functions, we may also hope to extract information on the collective structure of the rotational nuclear eigenstates from other measures of the wave function correlations, such as density distributions [24], spin and orbital angular momentum contributions [75], and symmetry decompositions [27]. In this regard, it is important to note that collective SU(3) correlations, consistent with the nuclear symplectic model, have been clearly demonstrated in calculations for ${}^6\text{Li}$, ${}^6\text{He}$, and ${}^8\text{Be}$, carried out directly in a symmetry-adapted SU(3)-based coupling scheme [21].

Acknowledgements

Discussions of experimental data with R. Smith, M. Freer, and Tz. Kokalova are gratefully acknowledged. We thank A. E. McCoy for comments on the manuscript. This material is based upon work supported by the US Department of Energy under Grants No. DE-FG02-95ER-40934, DESC0008485 (SciDAC/NUCLEI), and DE-FG02-87ER40371, and by the US National Science Foundation under Grant No. 0904782. This research used resources of the National Energy Research Scientific Computing Center (NERSC) and the Argonne Leadership Computing Facility (ALCF), which are U.S. Department of Energy Office of Science user facilities, supported under Contracts No. DE-AC02-05CH11231 and DE-AC02-06CH11357, and computing resources provided under the INCITE award “Nuclear Structure and Nuclear Reactions” from the U.S. Department of Energy, Office of Advanced Scientific Computing Research.

Appendix A: Single-particle estimate for intrinsic quadrupole moment

In heavier mass regions, rotational collectivity is commonly measured (*e.g.*, Refs. [3, 53]) by comparison of rotational transition strengths to the Weisskopf single-particle estimate. This is more properly a measure of the *number* of participating nucleons and of the quadrupole *deformation* of the intrinsic wave function, rather than of its *rotational* nature *per se*, *i.e.*, the separation of degrees of freedom embodied in (1). Nonetheless, it is worthwhile to keep the single-particle scale of transition strengths in mind, as this also provides a natural scale for the deviations from rotational strengths to be expected from

noncollective admixtures in rotational states.

Briefly, Weisskopf [45] estimates a typical scale $\mathcal{A} \approx e_{\frac{3}{5}}^3 (4\pi)^{-1/2} R^2$, for the matrix element $\langle \varphi_b | Q_{2\mu} | \varphi_a \rangle$ of the electric quadrupole operator for a single-particle transition between two states φ_a and φ_b , where we use $R = r_0 A^{1/3}$ with $r_0 = 1.2$ fm. This suggests the Weisskopf estimate $B_W \equiv \mathcal{A}^2$ for $B(E2)$ strengths, commonly termed the *Weisskopf unit* (W.u.).

However, quadrupole moments and $E2$ transition strengths vary greatly within a rotational band simply due to the angular momentum factors in (4) (see Fig. 1). Therefore, while one could choose one particular quadrupole moment $Q(J)$ or transition strength $B(E2; J \rightarrow J - \Delta J)$ within a band for comparison to Weisskopf's estimate (*e.g.*, the $2 \rightarrow 0$ transition strength is commonly quoted for $K = 0$ bands [76]), this comparison cannot be made consistently across bands of different K .

We therefore find it more meaningful to apply Weisskopf's estimate directly to the *intrinsic* matrix element of the quadrupole operator, *i.e.*, taking this to be of single-particle strength and seeing what magnitude this would imply for the *intrinsic* quadrupole moment Q_0 , thereby defining a single-particle scale relative to which enhancement can be judged.¹⁹ Taking $\langle \phi_K | Q_{20} | \phi_K \rangle \approx \mathcal{A}$ in (4) gives a single-particle estimate

$$Q_{0,W} = \frac{3}{5} \left(\frac{4}{5} \right)^{1/2} r_0^2 A^{2/3}. \quad (\text{A1})$$

For the Be isotopes considered here, the value of $Q_{0,W}$ ranges from $\sim 2.8 \text{ efm}^2$ for $A = 7$ to $\sim 4.1 \text{ efm}^2$ for $A = 12$. Of course, the traditional nuclear radius formula embodied in Weisskopf's estimate, and thus in (A1), is of only limited validity in these light nuclei.

-
- [1] D. J. Rowe, *Nuclear Collective Motion: Models and Theory* (World Scientific, Singapore, 2010).
 - [2] A. Bohr and B. R. Mottelson, *Nuclear Structure*, Vol. 1 (World Scientific, Singapore, 1998).
 - [3] A. Bohr and B. R. Mottelson, *Nuclear Structure*, Vol. 2 (World Scientific, Singapore, 1998).
 - [4] F. Iachello and A. Arima, *The Interacting Boson Model* (Cambridge University Press, Cambridge, 1987).

¹⁹ For instance, for a well-deformed rotational nucleus with $A \approx 150$, a typical value of $B(E2; 2 \rightarrow 0) \approx 100 \text{ W.u.}$ [76] thus corresponds to $Q_0/Q_{0,W} \approx 22$. Here we have used $B(E2; 2 \rightarrow 0) = (eQ_0)^2/(16\pi)$ for a $K = 0$ band, by (6).

- [5] J. M. Eisenberg and W. Greiner, *Nuclear Theory*, 3rd ed., Vol. 1 (North-Holland, Amsterdam, 1987).
- [6] J. P. Elliott, Proc. R. Soc. London A **245**, 128 (1958).
- [7] M. Harvey, Adv. Nucl. Phys. **1**, 67 (1968).
- [8] M. Horoi, B. A. Brown, T. Otsuka, M. Honma, and T. Mizusaki, Phys. Rev. C **73**, 061305 (2006).
- [9] S. C. Pieper, R. B. Wiringa, and J. Carlson, Phys. Rev. C **70**, 054325 (2004).
- [10] T. Neff and H. Feldmeier, Nucl. Phys. A **738**, 357 (2004).
- [11] G. Hagen, D. J. Dean, M. Hjorth-Jensen, T. Papenbrock, and A. Schwenk, Phys. Rev. C **76**, 044305 (2007).
- [12] S. Bacca, N. Barnea, and A. Schwenk, Phys. Rev. C **86**, 034321 (2012).
- [13] N. Shimizu, T. Abe, Y. Tsunoda, Y. Utsuno, T. Yoshida, T. Mizusaki, M. Honma, and T. Otsuka, Prog. Exp. Theor. Phys. **2012**, 01A205 (2012).
- [14] B. R. Barrett, P. Navrátil, and J. P. Vary, Prog. Part. Nucl. Phys. **69**, 131 (2013).
- [15] P. Navrátil, J. P. Vary, and B. R. Barrett, Phys. Rev. Lett. **84**, 5728 (2000).
- [16] P. Maris, J. P. Vary, and A. M. Shirokov, Phys. Rev. C **79**, 014308 (2009).
- [17] R. Roth and P. Navrátil, Phys. Rev. Lett. **99**, 092501 (2007).
- [18] R. Roth, Phys. Rev. C **79**, 064324 (2009).
- [19] T. Abe, P. Maris, T. Otsuka, N. Shimizu, Y. Utsuno, and J. P. Vary, Phys. Rev. C **86**, 054301 (2012).
- [20] T. Dytrych, K. D. Sviratcheva, J. P. Draayer, C. Bahri, and J. P. Vary, J. Phys. G **35**, 123101 (2008).
- [21] T. Dytrych, K. D. Launey, J. P. Draayer, P. Maris, J. P. Vary, E. Saule, U. Catalyurek, M. Sosonkina, D. Langr, and M. A. Caprio, Phys. Rev. Lett. **111**, 252501 (2013).
- [22] P. Navrátil, S. Quaglioni, I. Stetcu, and B. R. Barrett, J. Phys. G **36**, 083101 (2009).
- [23] S. K. Bogner, R. J. Furnstahl, P. Maris, R. J. Perry, A. Schwenk, and J. Vary, Nucl. Phys. A **801**, 21 (2008).
- [24] C. Cockrell, J. P. Vary, and P. Maris, Phys. Rev. C **86**, 034325 (2012).
- [25] R. B. Wiringa, S. C. Pieper, J. Carlson, and V. R. Pandharipande, Phys. Rev. C **62**, 014001 (2000).
- [26] T. Dytrych, K. D. Sviratcheva, C. Bahri, J. P. Draayer, and J. P. Vary, Phys. Rev. C **76**,

- 014315 (2007).
- [27] T. Dytrych, K. D. Sviratcheva, C. Bahri, J. P. Draayer, and J. P. Vary, *J. Phys. G* **35**, 095101 (2008).
 - [28] T. Neff and H. Feldmeier, *Eur. Phys. J. Special Topics* **156**, 69 (2008).
 - [29] P. Maris, *J. Phys. Conf. Ser.* **402**, 012031 (2012).
 - [30] A. M. Shirokov, J. P. Vary, A. I. Mazur, and T. A. Weber, *Phys. Lett. B* **644**, 33 (2007).
 - [31] M. A. Caprio, P. Maris, and J. P. Vary, *Phys. Lett. B* **719**, 179 (2013).
 - [32] J. D. Rogers, *Annu. Rev. Nucl. Sci.* **15**, 241 (1965).
 - [33] A. R. Edmonds, *Angular Momentum in Quantum Mechanics*, 2nd ed., Investigations in Physics No. 4 (Princeton University Press, Princeton, New Jersey, 1960).
 - [34] D. A. Varshalovich, A. N. Moskalev, and V. K. Khersonskii, *Quantum Theory of Angular Momentum* (World Scientific, Singapore, 1988).
 - [35] J. Suhonen, *From Nucleons to Nucleus* (Springer-Verlag, Berlin, 2007).
 - [36] P. Maris and J. P. Vary, *Int. J. Mod. Phys. E* **22**, 1330016 (2013).
 - [37] A. M. Shirokov, V. A. Kulikov, P. Maris, and J. P. Vary, in *NN and 3N Interactions*, edited by L. D. Blokhintsev and I. I. Strakovsky (Nova Science, Hauppauge, N.Y., 2014), Chap. 8.
 - [38] R. R. Whitehead, A. Watt, B. J. Cole, and I. Morrison, *Adv. Nucl. Phys.* **9**, 123 (1977).
 - [39] P. Sternberg, E. G. Ng, C. Yang, P. Maris, J. P. Vary, M. Sosonkina, and H. V. Le, in *SC '08: Proceedings of the 2008 ACM/IEEE Conference on Supercomputing* (IEEE Press, Piscataway, NJ, 2008), Article No. 15.
 - [40] P. Maris, M. Sosonkina, J. P. Vary, E. Ng, and C. Yang, *Procedia Comput. Sci.* **1**, 97 (2010).
 - [41] H. M. Aktulga, C. Yang, E. G. Ng, P. Maris, and J. P. Vary, *Concurrency Computat.: Pract. Exper.* **16**, 2631 (2013).
 - [42] F. Ajzenberg-Selove, *Nucl. Phys. A* **506**, 1 (1990).
 - [43] C. Lanczos, *J. Res. Natl. Bur. Stand.* **45**, 255 (1950).
 - [44] K. Alder and A. Winther, *Electromagnetic Excitation* (North-Holland, Amsterdam, 1975).
 - [45] V. F. Weisskopf, *Phys. Rev.* **83**, 1073 (1951).
 - [46] D. R. Tilley, C. M. Cheves, J. L. Godwin, G. M. Hale, H. M. Hofmann, J. H. Kelley, C. G. Sheu, and H. R. Weller, *Nucl. Phys. A* **708**, 3 (2002).
 - [47] D. R. Tilley, J. H. Kelley, J. L. Godwin, D. J. Millener, J. E. Purcell, C. G. Sheu, and H. R. Weller, *Nucl. Phys. A* **745**, 155 (2004).

- [48] V. M. Datar, D. R. Chakrabarty, S. Kumar, V. Nanal, S. Pastore, R. B. Wiringa, S. P. Behera, A. Chatterjee, D. Jenkins, C. J. Lister, E. T. Mirgule, A. Mitra, R. G. Pillay, K. Ramachandran, O. J. Roberts, P. C. Rout, A. Shrivastava, and P. Sugathan, *Phys. Rev. Lett.* **111**, 062502 (2013).
- [49] S. A. Coon, M. I. Avetian, M. K. G. Kruse, U. van Kolck, P. Maris, and J. P. Vary, *Phys. Rev. C* **86**, 054002 (2012).
- [50] R. J. Furnstahl, G. Hagen, and T. Papenbrock, *Phys. Rev. C* **86**, 031301 (2012).
- [51] J. P. Draayer, K. J. Weeks, and G. Rosensteel, *Nucl. Phys. A* **413**, 215 (1984).
- [52] D. J. Rowe, *Rep. Prog. Phys.* **48**, 1419 (1985).
- [53] R. F. Casten, *Nuclear Structure from a Simple Perspective*, 2nd ed., Oxford Studies in Nuclear Physics No. 23 (Oxford University Press, Oxford, 2000).
- [54] Y. Kanada-En'yo, H. Horiuchi, and A. Doté, *Phys. Rev. C* **1999**, 064304 (1999).
- [55] W. von Oertzen, *Z. Phys. A* **354**, 37 (1996).
- [56] W. von Oertzen, *Z. Phys. A* **357**, 355 (1997).
- [57] D. Suzuki, A. Shore, W. Mittig, J. J. Kolata, D. Bazin, M. Ford, T. Ahn, D. Becchetti, S. Beceiro Novo, D. Ben Ali, B. Bucher, J. Browne, X. Fang, M. Febraro, A. Fritsch, E. Galyaev, A. M. Howard, N. Keeley, W. G. Lynch, M. Ojaruega, A. L. Roberts, and X. D. Tang, *Phys. Rev. C* **87**, 054301 (2013).
- [58] H. G. Bohlen, W. von Oertzen, R. Kalpakchieva, T. N. Massey, T. Corsch, M. Milin, C. Schulz, Tz. Kokalova, and C. Wheldon, *J. Phys. Conf. Ser.* **111**, 012021 (2008).
- [59] S. G. Nilsson, *Mat. Fys. Medd. Dan. Vid. Selsk.* **29**(16) (1955).
- [60] B. R. Mottelson and S. G. Nilsson, *Mat. Fys. Skr. Dan. Vid. Selsk.* **1**(8) (1959).
- [61] I. Ragnarsson, S. Åberg, H.-B. Høakansson, and R. K. Sheline, *Nucl. Phys. A* **361**, 1 (1981).
- [62] H. Bohlen, A. Blažević, B. Gebauer, S. M. Grimes, R. Kalpakchieva, T. N. Massey, W. von Oertzen, S. Thummerer, and M. Wilpert, *AIP Conf. Proc.* **495**, 303 (1999).
- [63] M. Freer, J. C. Angélique, L. Axelsson, B. Benoit, U. Bergmann, W. N. Catford, S. P. G. Chappell, N. M. Clarke, N. Curtis, A. D'Arrigo, E. de Goes Brennard, O. Dorvaux, B. R. Fulton, G. Giardina, C. Gregori, S. Grévy, F. Hanappe, G. Kelly, M. Labiche, C. Le Brun, S. Leenhardt, M. Lewitowicz, K. Markenroth, F. M. Marqués, M. Motta, J. T. Murgatroyd, T. Nilsson, A. Ninane, N. A. Orr, I. Piqueras, M. G. Saint Laurent, S. M. Singer, O. Sorlin, L. Stuttgé, and D. L. Watson, *Phys. Rev. Lett.* **82**, 1383 (1999).

- [64] H. T. Fortune, G.-B. Liu, and D. E. Alburger, *Phys. Rev. C* **50**, 1355 (1994).
- [65] H. G. Bohlen, R. Kalpakchieva, W. von Oertzen, T. N. Massey, B. Gebauer, T. Kokalova, A. A. Ogloblind, Ch. Schulz, and S. Thummerer, *Nucl. Phys. A* **738**, 333 (2004).
- [66] H. G. Bohlen, W. von Oertzen, Tz. Kokalova, Ch. Schulz, R. Kalpakchieva, T. N. Massey, and M. Milin, *Int. J. Mod. Phys. E* **17**, 2067 (2008).
- [67] F. C. Barker, *J. Phys. G* **2**, L45 (1976).
- [68] A. Navin, D. W. Anthony, T. Aumann, T. Baumann, D. Bazin, Y. Blumenfeld, B. A. Brown, T. Glasmacher, P. G. Hansen, R. W. Ibbotson, P. A. Lofy, V. Maddalena, K. Miller, T. Nakamura, B. V. Pritychenko, B. M. Sherrill, E. Spears, M. Steiner, J. A. Tostevin, J. Yurkon, and A. Wagner, *Phys. Rev. Lett.* **85**, 266 (2000).
- [69] S. D. Pain, W. N. Catford, N. A. Orr, J. C. Angélique, N. I. Ashwood, V. Bouchat, N. M. Clarke, N. Curtis, M. Freer, B. R. Fulton, F. Hanappe, M. Labiche, J. L. Lecouey, R. C. Lemmon, D. Mahboub, A. Ninane, G. Normand, N. Soić, L. Stuttge, C. N. Timis, J. A. Tostevin, J. S. Winfield, , and V. Ziman, *Phys. Rev. Lett.* **96**, 032502 (2006).
- [70] R. Kanungo, A. T. Gallant, M. Uchida, C. Andreoiu, R. A. E. Austin, D. Bandyopadhyay, G. C. Ball, J. A. Becker, A. J. Boston, H. C. Boston, B. A. Brown, L. Buchmann, S. J. Colosimo, R. M. Clark, D. Cline, D. S. Cross, H. Dare, B. Davids, T. E. Drake, M. Djongolov, P. Finlay, N. Galinski, P. E. Garrett, A. B. Garnsworthy, K. L. Green, S. Grist, G. Hackman, L. J. Harkness, A. B. Hayes, D. Howell, A. M. Hurst, H. B. Jeppesen, K. G. Leach, A. O. Macchiavelli, D. Oxley, C. J. Pearson, B. Pietras, A. A. Phillips, S. V. Rigby, C. Ruiz, G. Ruprecht, F. Sarazin, M. A. Schumaker, A. C. Shotter, C. S. Sumitharachchi, C. E. Svensson, I. Tanihata, S. Triambak, C. Unsworth, S. J. Williams, P. Walden, J. Wong, and C. Y. Wu, *Phys. Lett. B* **682**, 391 (2010).
- [71] R. Meharchand, R. G. T. Zegers, B. A. Brown, S. M. Austin, T. Baugher, D. Bazin, J. Deaven, A. Gade, G. F. Grinyer, C. J. Guess, M. E. Howard, H. Iwasaki, S. McDaniel, K. Meierbachtol, G. Perdikakis, J. Pereira, A. M. Prinke, A. Ratkiewicz, A. Signoracci, S. Stroberg, L. Valdez, P. Voss, K. A. Walsh, D. Weisshaar, and R. Winkler, *Phys. Rev. Lett.* **108**, 122501 (2012).
- [72] P. Maris, H. M. Aktulga, M. A. Caprio, U. V. Catalyurek, E. Ng, D. Oryspayev, H. Potter, E. Saule, M. Sosonkina, J. P. Vary, C. Yang, and Z. Zhou, *J. Phys. Conf. Ser.* **403**, 012019 (2012).
- [73] P. Maris, H. M. Aktulga, S. Binder, A. Calci, Ü. V. Çatalyürek, J. Langhammer, E. Ng,

- E. Saule, R. Roth, J. P. Vary, and C. Yang, J. Phys. Conf. Ser. **454**, 012063 (2013).
- [74] M. Pervin, S. C. Pieper, and R. B. Wiringa, Phys. Rev. C **76**, 064319 (2007).
- [75] C. W. Johnson, arXiv:1203.2515.
- [76] S. Raman, C. W. Nestor, Jr., and P. Tikkanen, At. Data Nucl. Data Tables **78**, 1 (2001).
- [77] H. G. Bohlen, R. Kalpakchieva, W. von Oertzen, T. N. Massey, B. G. S. M. Grimes, T. Kokalova, H. Lenske, A. Lenz, M. Milin, Ch. Schulz, S. Thummerer, S. Torilov, and A. Tumino, Nucl. Phys. A **722**, 3c (2003).
- [78] H. G. Bohlen, A. Blazevic, B. Gebauer, W. von Oertzen, S. Thummerer, R. Kalpakchieva, S. M. Grimes, and T. N. Massey, Prog. Part. Nucl. Phys. **42**, 17 (1999).
- [79] H. G. Bohlen, T. Dorsch, Tz. Kokalova, W. von Oertzen, Ch. Schulz, , and C. Wheldon, Phys. Rev. C **75**, 054604 (2007).
- [80] M. Freer, E. Casarejos, L. Achouri, C. Angulo, N. I. Ashwood, N. Curtis, P. Demaret, C. Harlin, B. Laurent, M. Milin, N. A. Orr, D. Price, R. Raabe, N. Soić, and V. A. Ziman, Phys. Rev. Lett. **96**, 042501 (2006).
- [81] S. Shimoura, A. Saitob, T. Minemura, Y. Matsuyama, H. Baba, H. Akiyoshi, N. Aoi, T. Gomi, Y. Higurashi, K. Ieki, N. Imai, N. Iwasa, H. Iwasaki, S. Kanno, S. Kubono, M. Kunibu, S. Michimasa, T. Motobayashi, T. Nakamura, H. Sakurai, M. Serata, E. Takeshita, S. Takeuchi, T. Teranishi, K. Ue, K. Yamada, Y. Yanagisawa, M. Ishihara, and N. Itagaki, Phys. Lett. B **560**, 31 (2003).

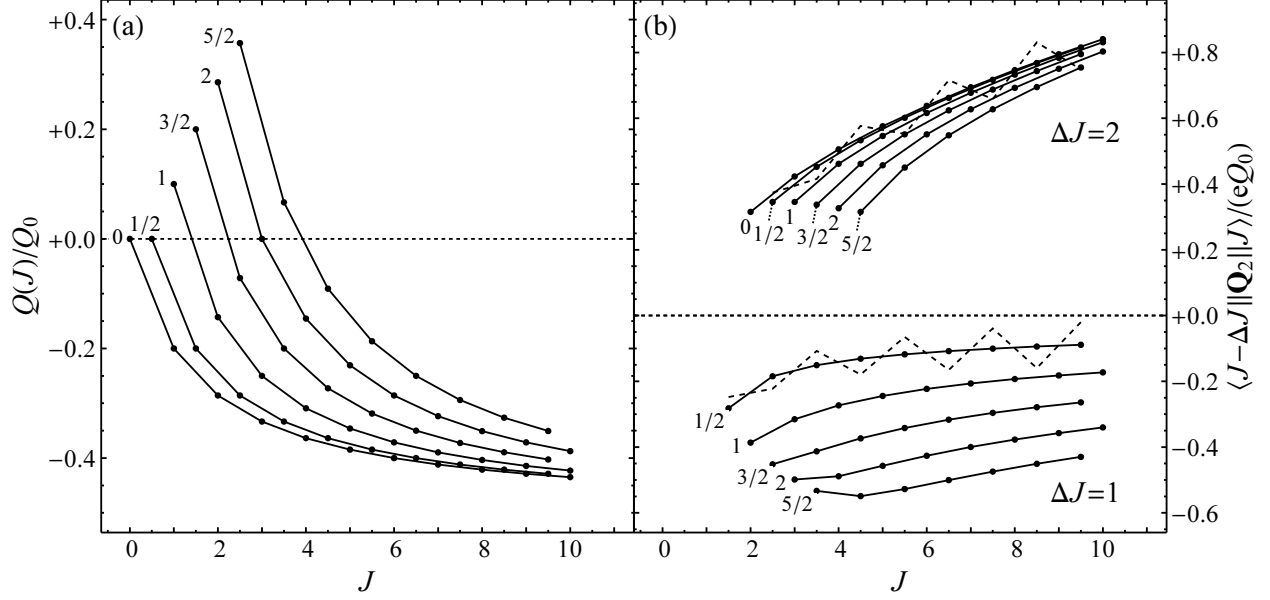


FIG. 1: Rotational predictions for (a) electric quadrupole moments and (b) electric quadrupole transition reduced matrix elements, within a rotational band, normalized to the intrinsic quadrupole moment Q_0 , following from (4). Predictions are shown for bands with $0 \leq K \leq 5/2$, as indicated. The staggering induced in transitions within a $K = 1/2$ band, taking $\langle \phi_K | Q_{2,2K} | \phi_{\bar{K}} \rangle / \langle \phi_K | Q_{2,0} | \phi_K \rangle = +0.1$ for illustration, is indicated by the dotted lines.

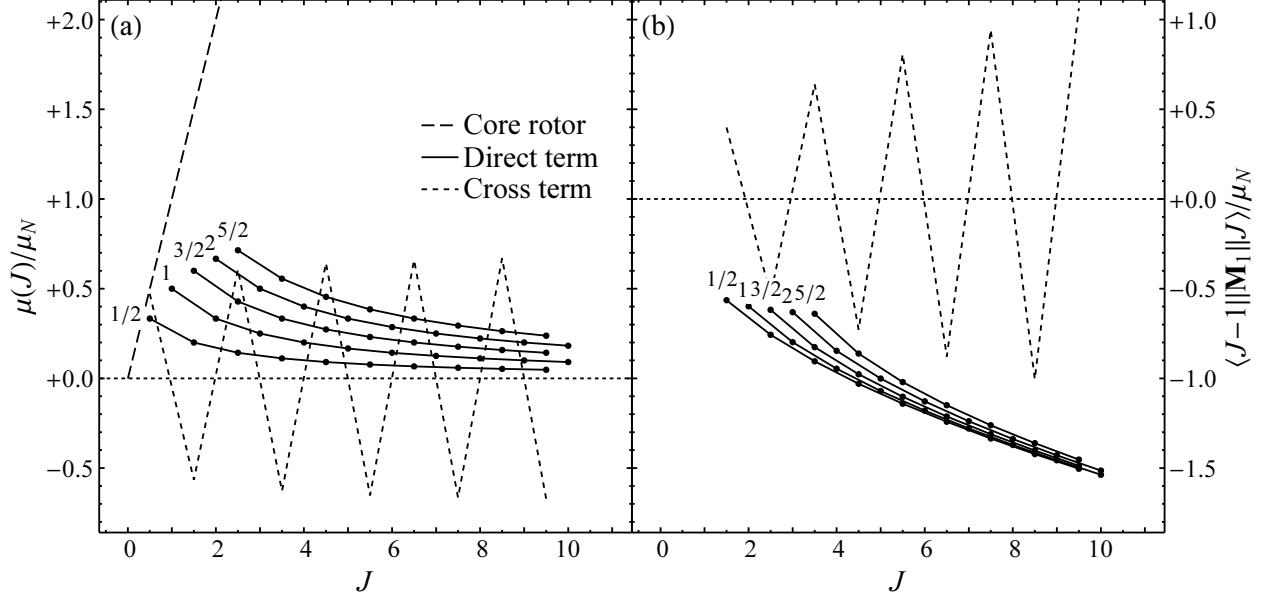


FIG. 2: Rotational predictions for each of the terms contributing, in (10) and (11), to (a) magnetic dipole moments and (b) magnetic dipole transition reduced matrix elements, within a rotational band: the core rotor term for dipole moments (dashed line), direct term (solid lines, $K \geq 1/2$ only, as indicated), and cross term (dotted lines, $K = 1/2$ only). For purposes of comparison, these terms are shown with equal coefficients, *i.e.*, with $a_1 = a_2 = a_3 = \mu_N$. Predictions are shown for bands with $0 \leq K \leq 5/2$.

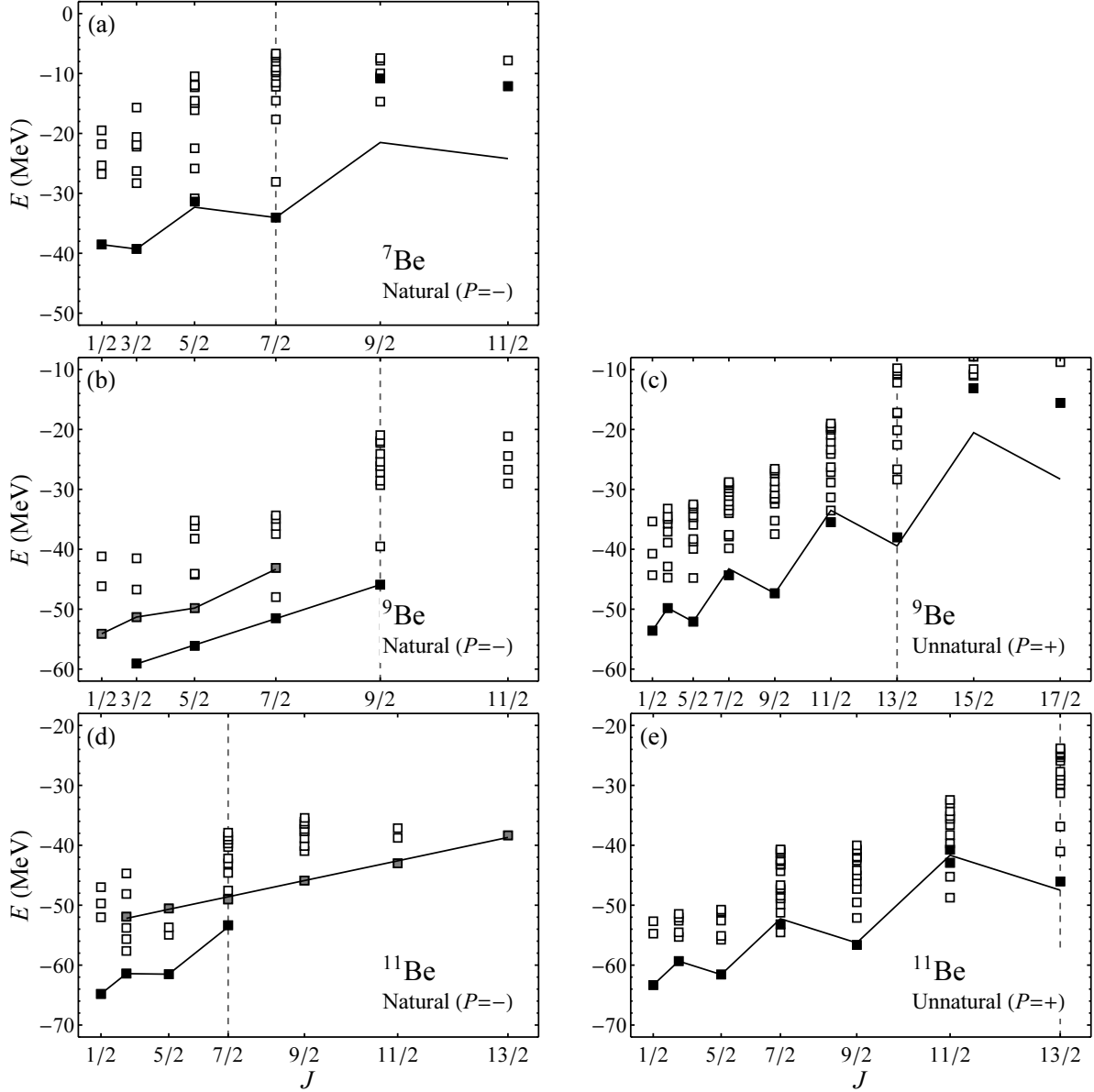


FIG. 3: Energy eigenvalues obtained for states in the natural (left) and unnatural (right) parity spaces of the odd-mass Be isotopes ($7 \leq A \leq 11$). Energies are plotted with respect to an angular momentum axis which is scaled to be linear in $J(J+1)$, to facilitate identification of rotational energy patterns. Filled symbols indicate candidate rotational band members (black for yrast band members and shaded for excited band members). The lines indicate the corresponding best fits for rotational energies (see text). Where quadrupole transition strengths indicate significant fragmentation, more than one state of a given J may be indicated as a band member. The vertical dashed lines indicate the maximal angular momentum accessible within the lowest harmonic oscillator configuration (or valence space).

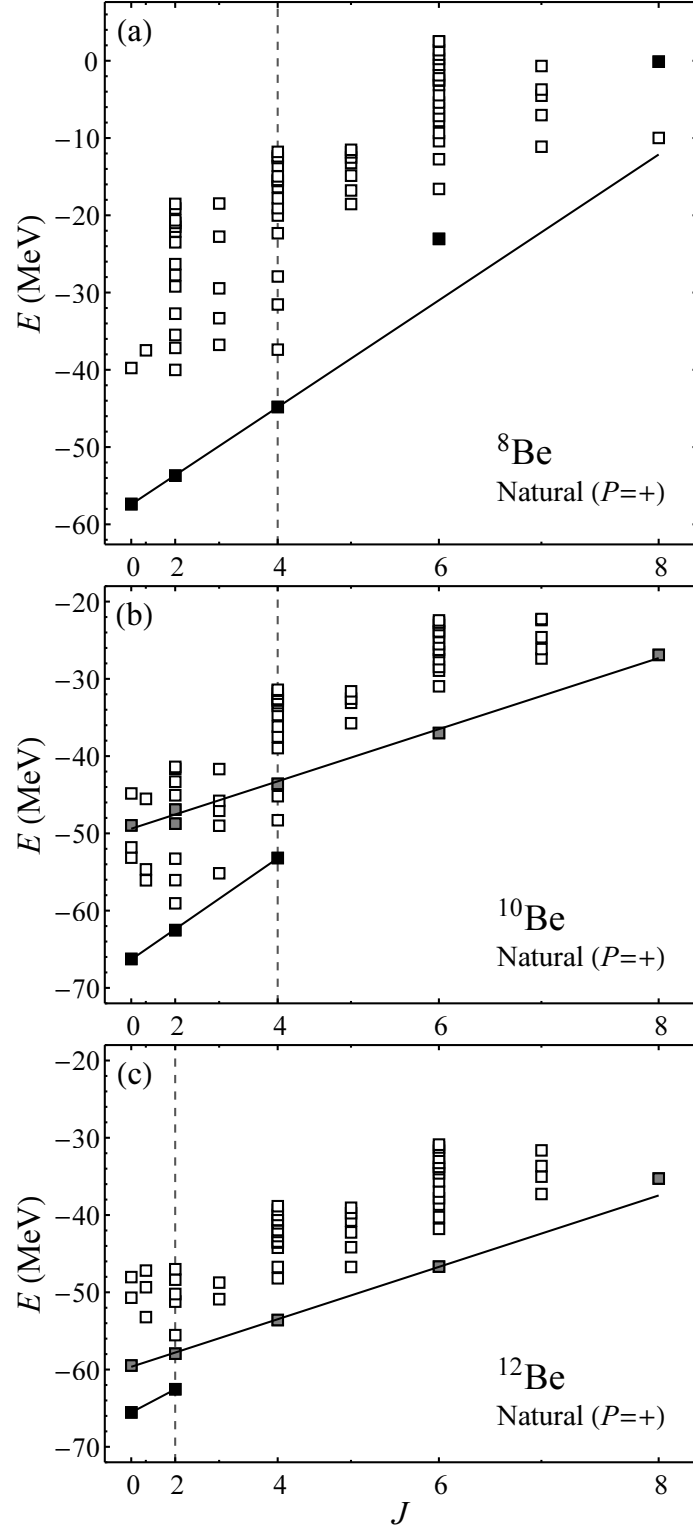


FIG. 4: Energy eigenvalues obtained for states in the *natural* parity spaces of the even-mass Be isotopes ($8 \leq A \leq 12$). See Fig. 3 caption for discussion of the plot contents and labeling.

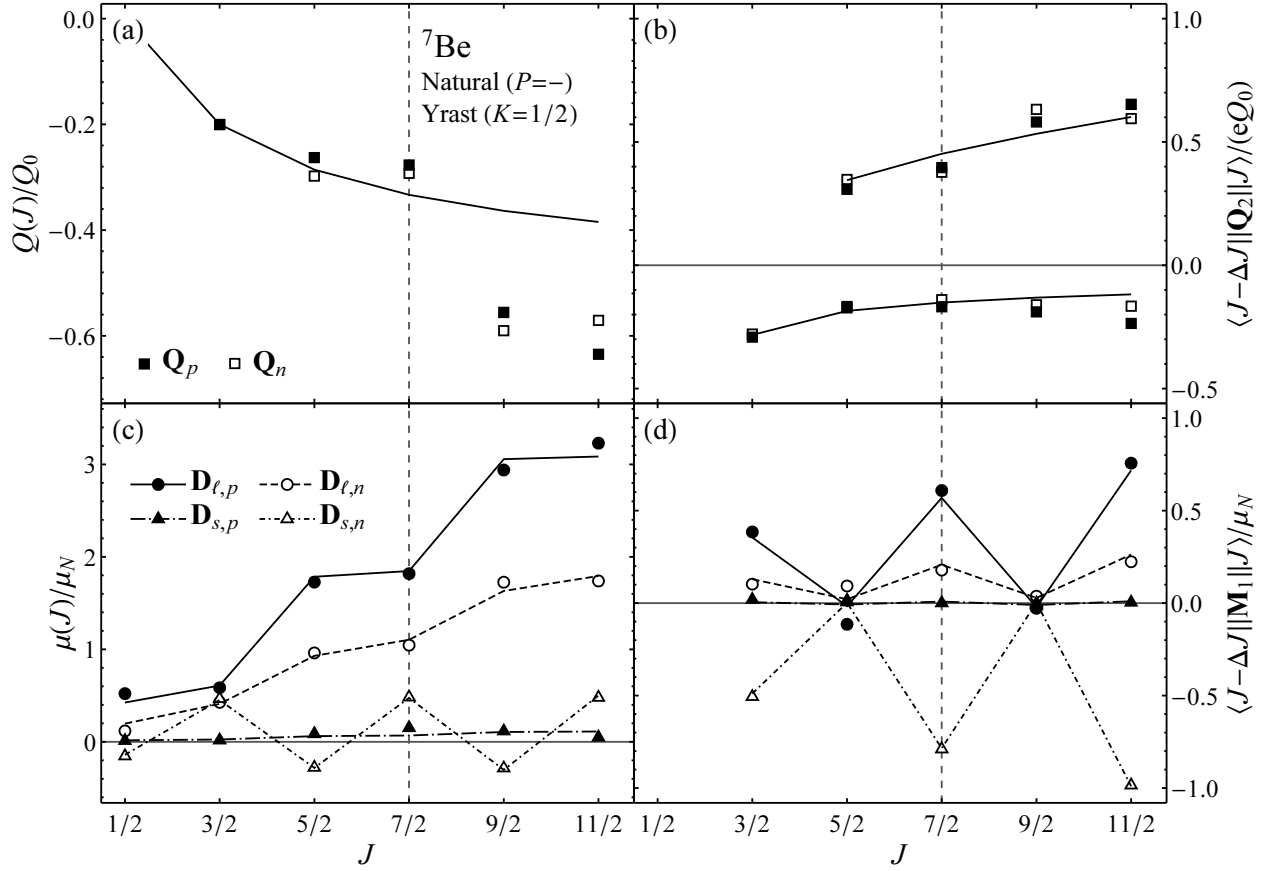


FIG. 5: Dipole and quadrupole matrix element observables for the ${}^7\text{Be}$ natural parity yrast band: (a) quadrupole ($E2$) moments, (b) quadrupole transition reduced matrix elements, (c) dipole ($M1$) moments, and (d) dipole transition reduced matrix elements. For quadrupole moments and matrix elements, values calculated using both proton and neutron operators are shown. Similarly, for dipole moments and matrix elements, values calculated using all four dipole terms (*i.e.*, proton/neutron and orbital/spin contributions) are shown. Quadrupole moments and matrix elements are normalized to Q_0 , obtained from the lowest band member's quadrupole moment. The curves indicate the rotational values for the quadrupole moments and matrix elements (normalized to Q_0) and for the dipole moments and matrix elements (using band best-fit parameters obtained from the dipole moments). The vertical dashed lines indicate the maximal angular momentum accessible within the lowest harmonic oscillator configuration (or valence space).

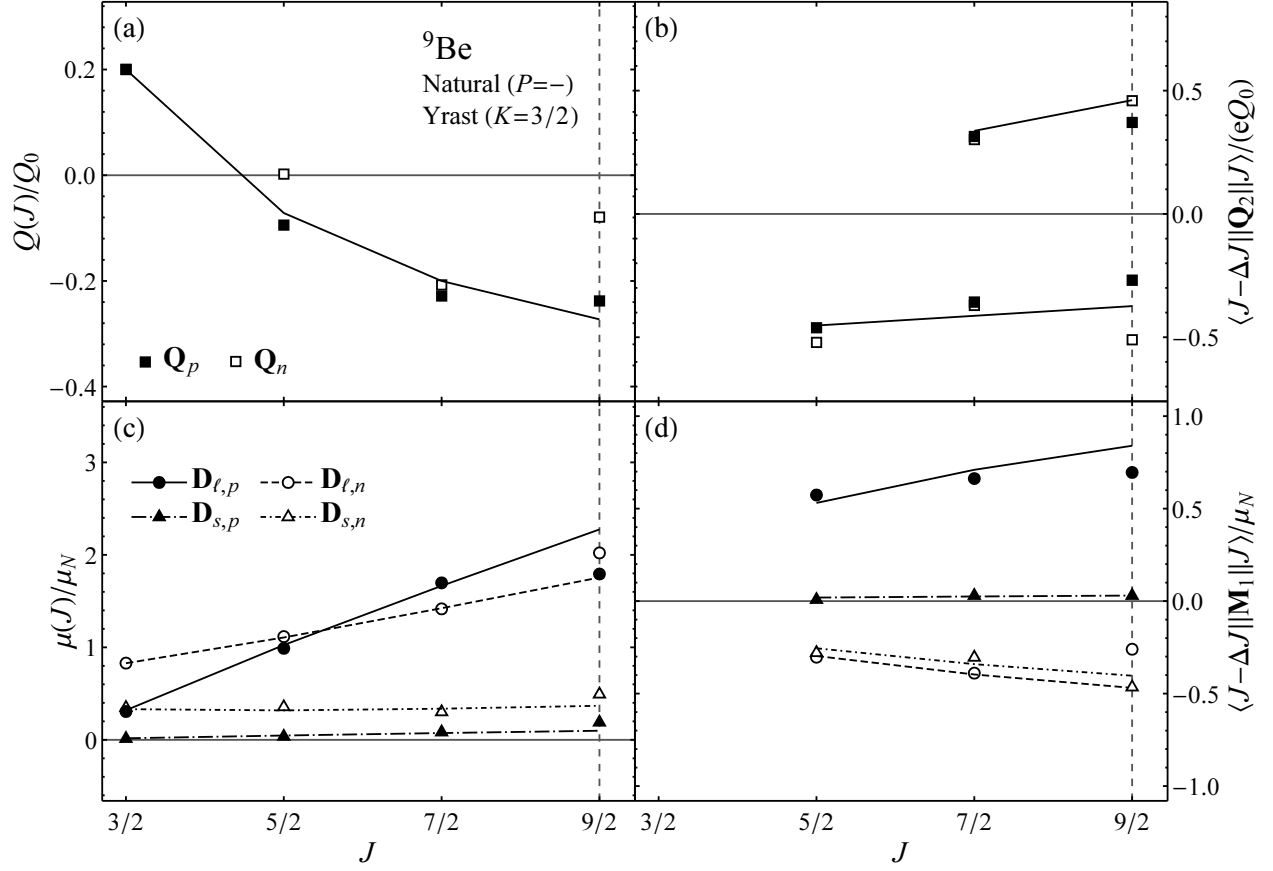


FIG. 6: Dipole and quadrupole matrix element observables for the ${}^9\text{Be}$ natural parity yrast band. See Fig. 5 caption for discussion of the plot contents and labeling.

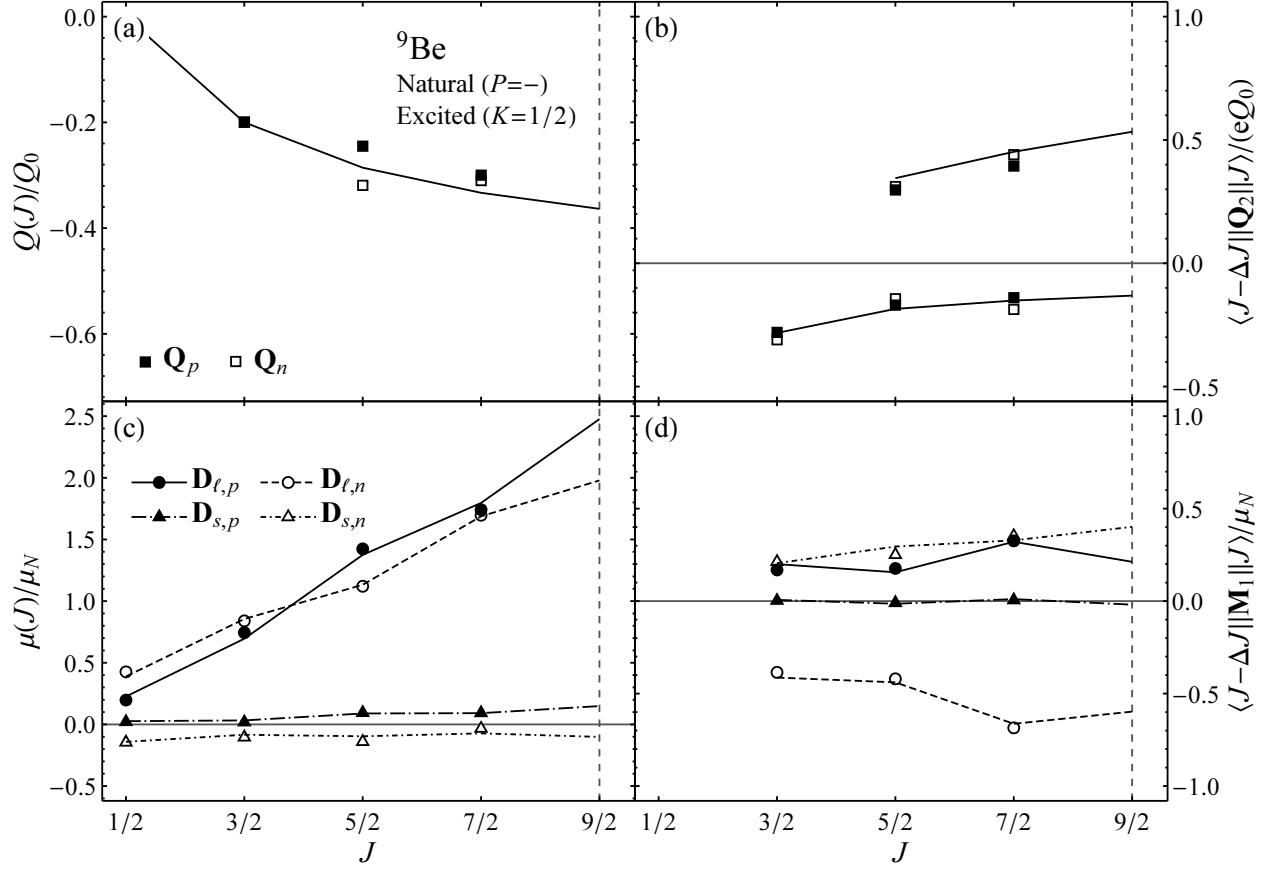


FIG. 7: Dipole and quadrupole matrix element observables for the ${}^9\text{Be}$ natural parity excited band. See Fig. 5 caption for discussion of the plot contents and labeling.

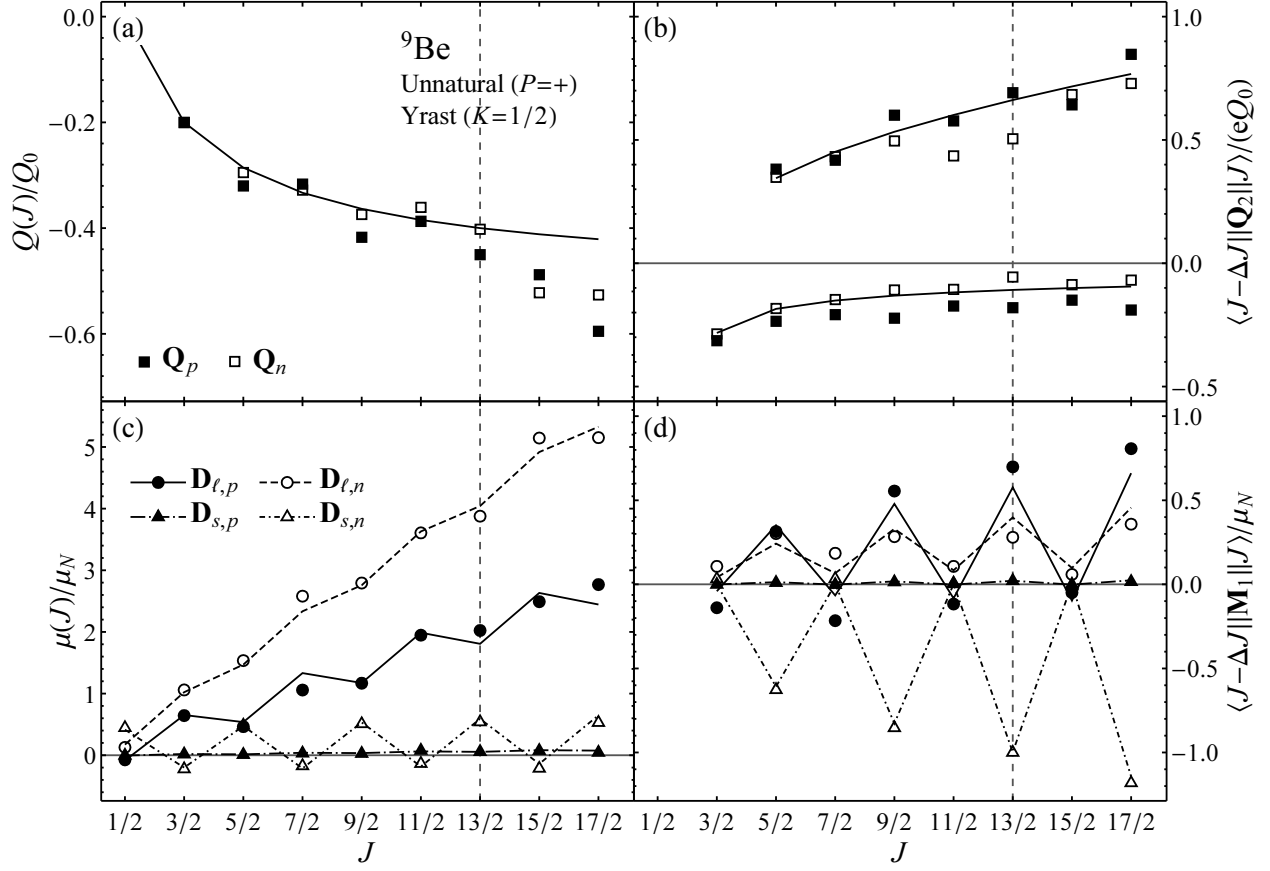


FIG. 8: Dipole and quadrupole matrix element observables for the ${}^9\text{Be}$ unnatural parity yrast band. See Fig. 5 caption for discussion of the plot contents and labeling.

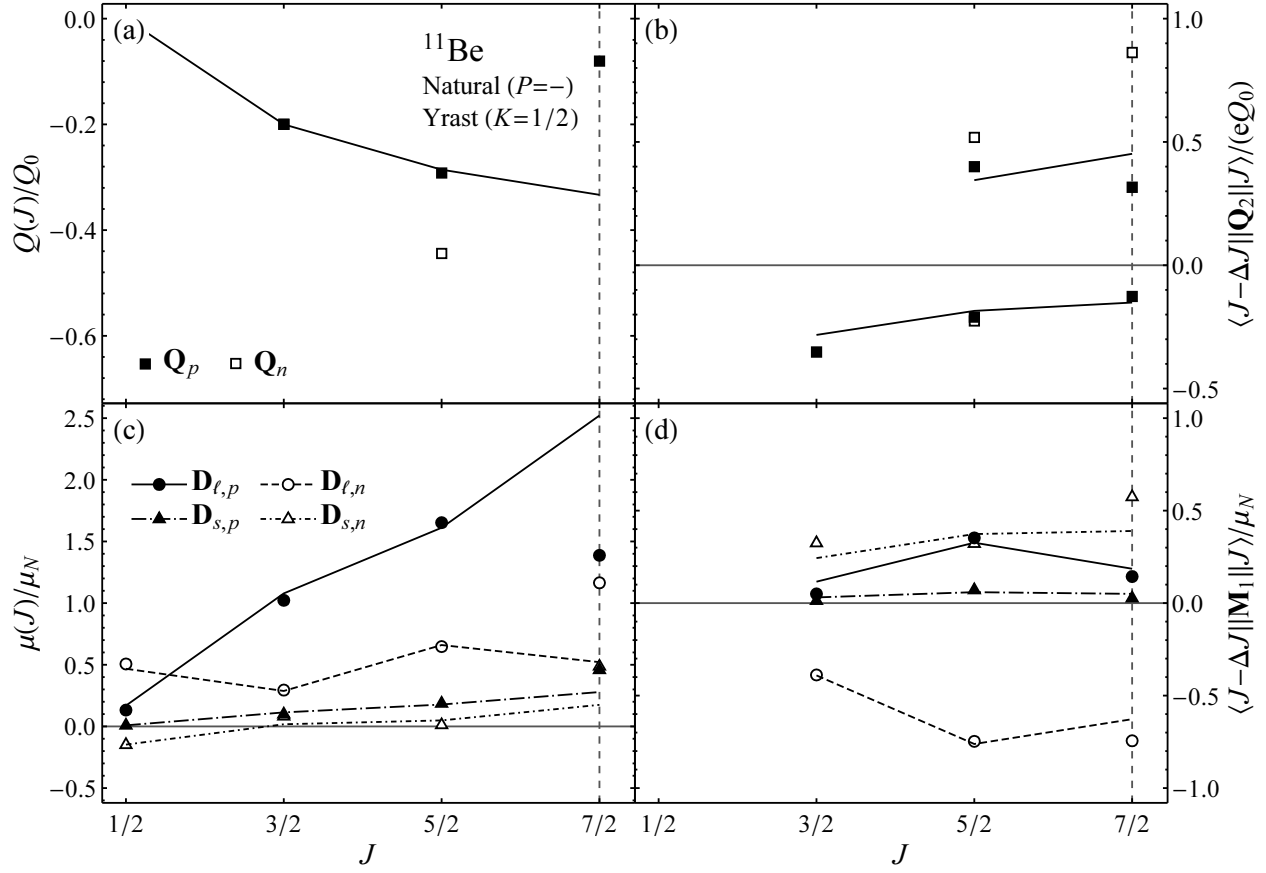


FIG. 9: Dipole and quadrupole matrix element observables for the ^{11}Be natural parity yrast band. See Fig. 5 caption for discussion of the plot contents and labeling.

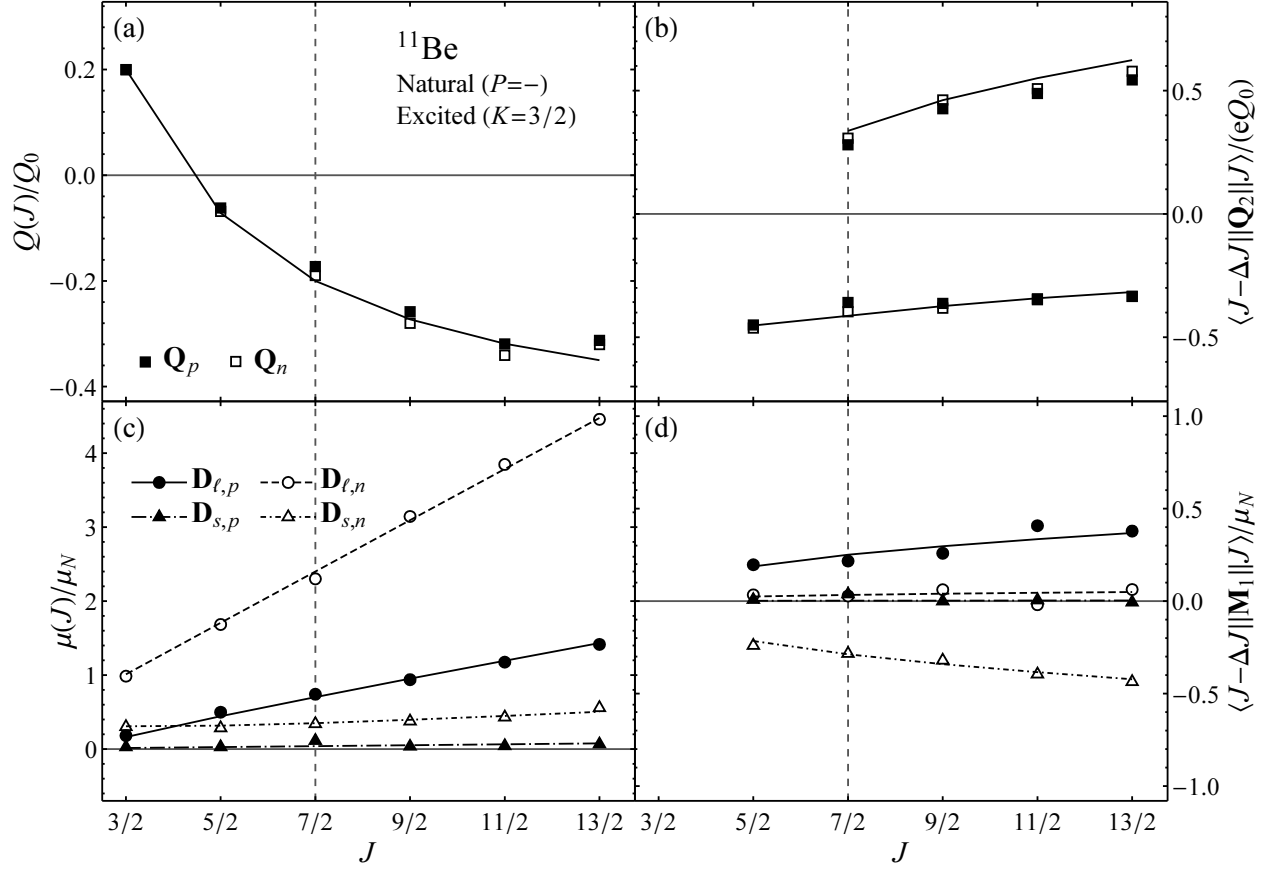


FIG. 10: Dipole and quadrupole matrix element observables for the ^{11}Be natural parity excited band. See Fig. 5 caption for discussion of the plot contents and labeling.

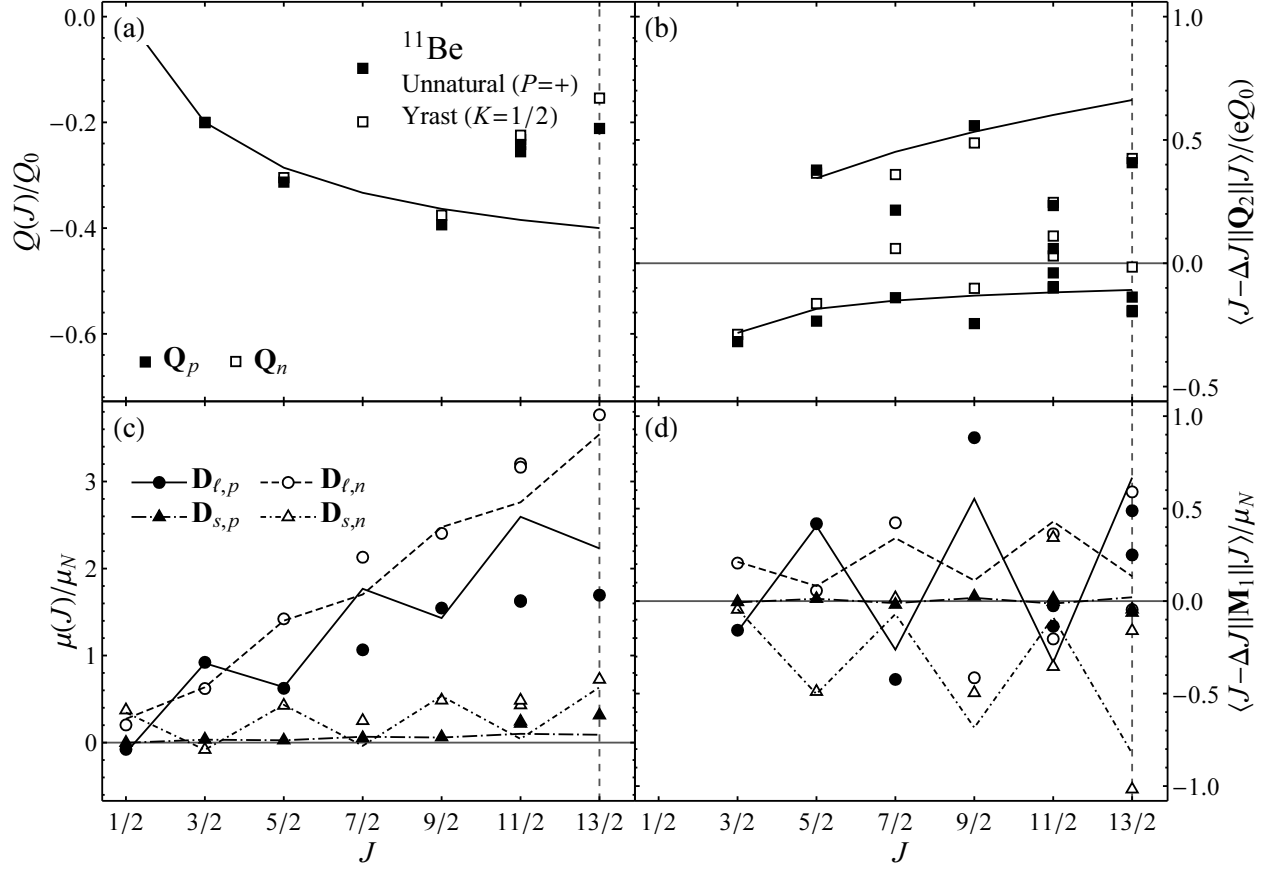


FIG. 11: Dipole and quadrupole matrix element observables for the ^{11}Be unnatural parity yrast band. See Fig. 5 caption for discussion of the plot contents and labeling.

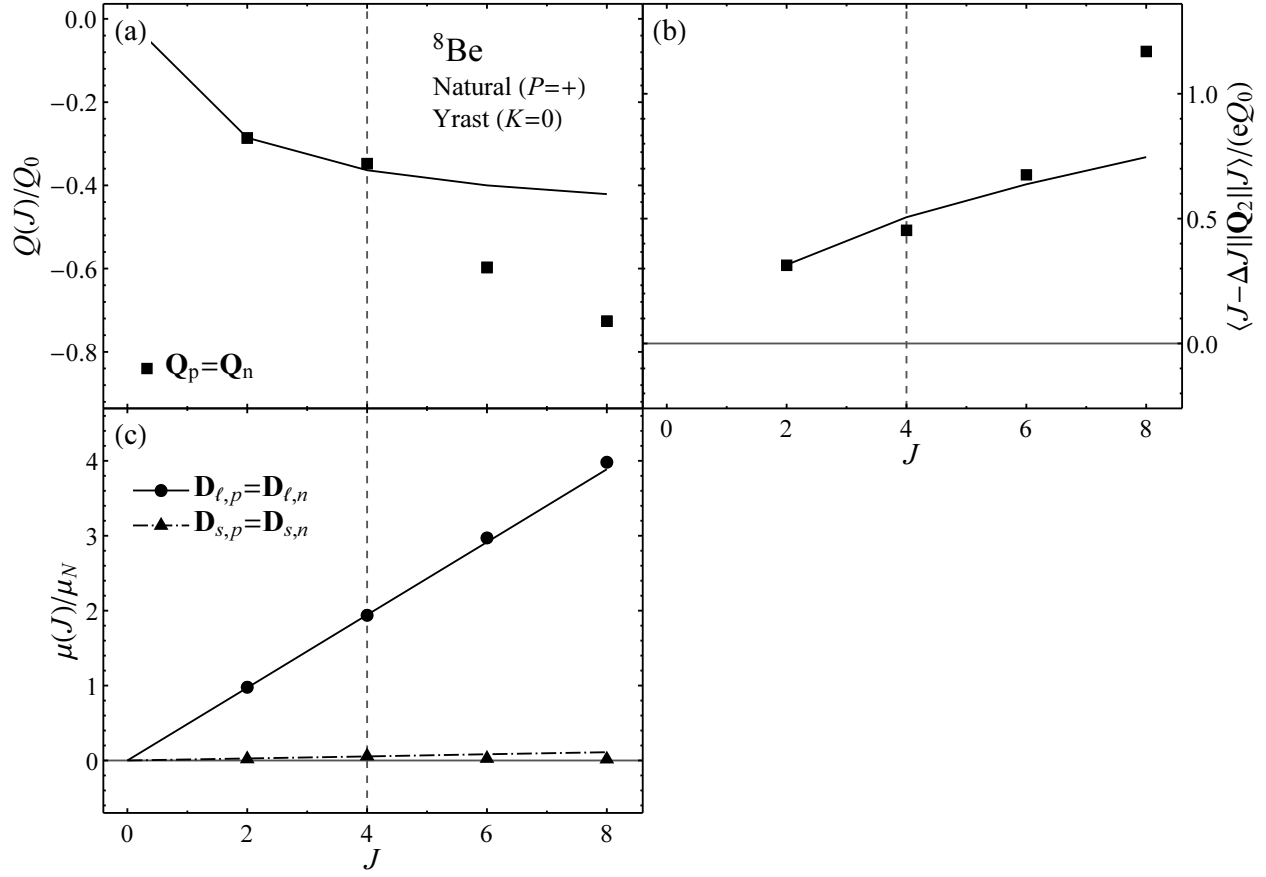


FIG. 12: Dipole and quadrupole matrix element observables for the ^8Be natural parity yrast band. See Fig. 5 caption for discussion of the plot contents and labeling. Proton and neutron observables are identical due to isospin symmetry for ^8Be .

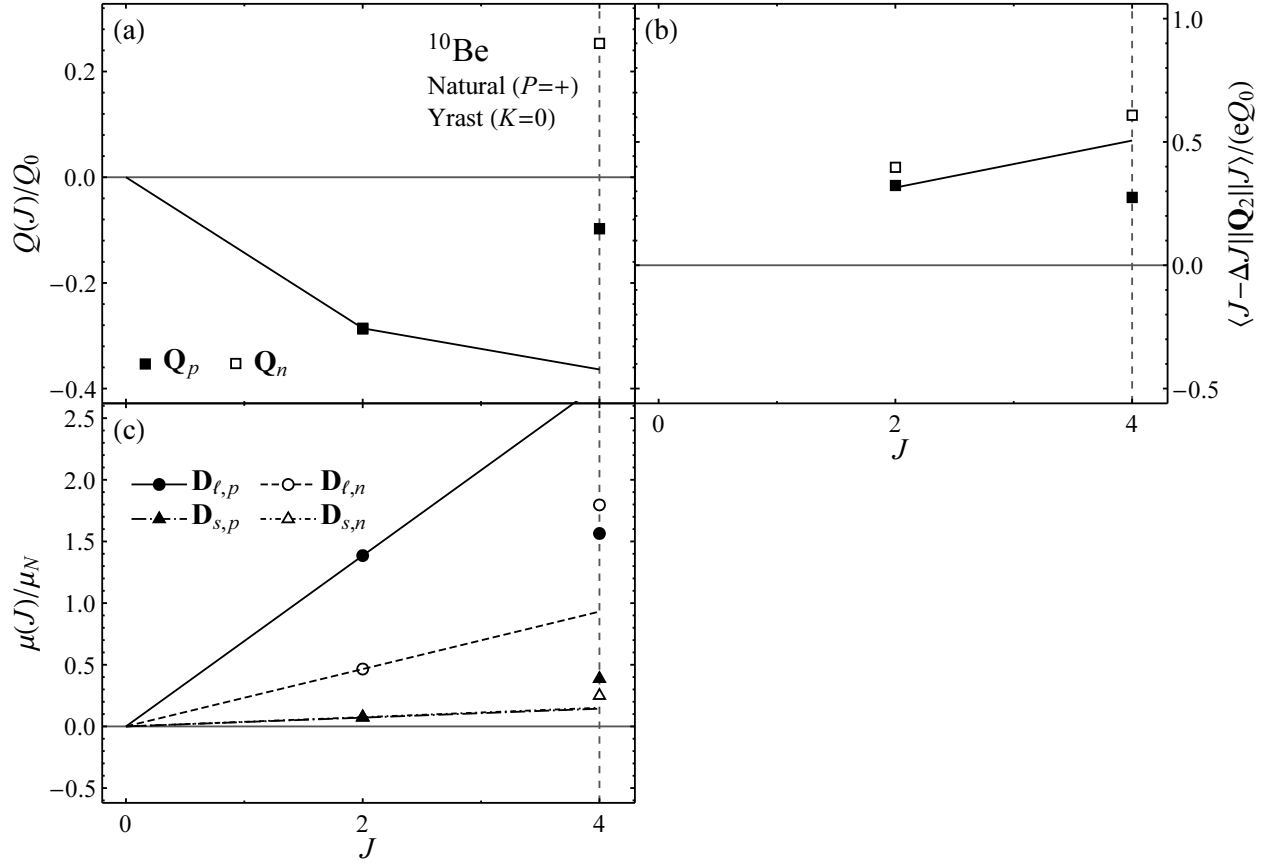


FIG. 13: Dipole and quadrupole matrix element observables for the ^{10}Be natural parity yrast band. See Fig. 5 caption for discussion of the plot contents and labeling.

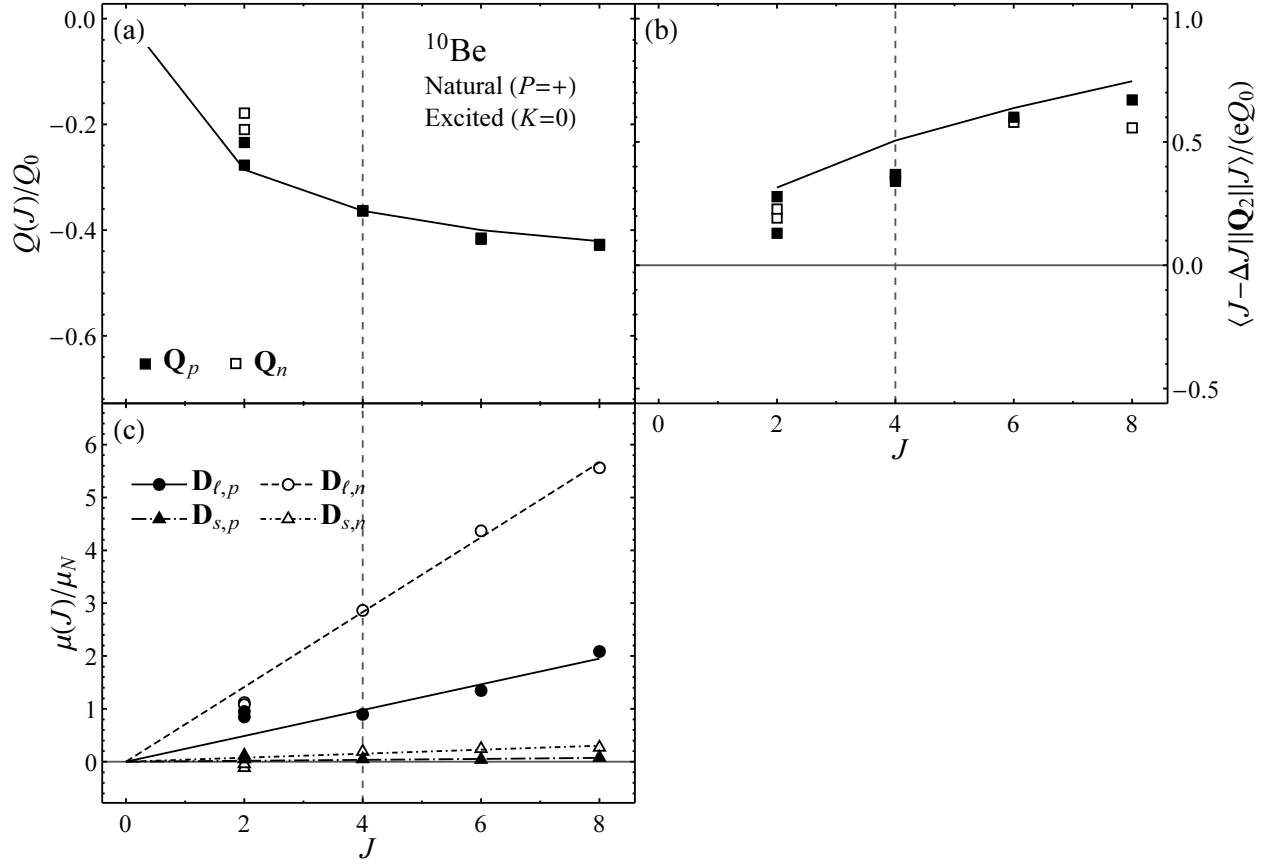


FIG. 14: Dipole and quadrupole matrix element observables for the ^{10}Be natural parity excited band. See Fig. 5 caption for discussion of the plot contents and labeling.

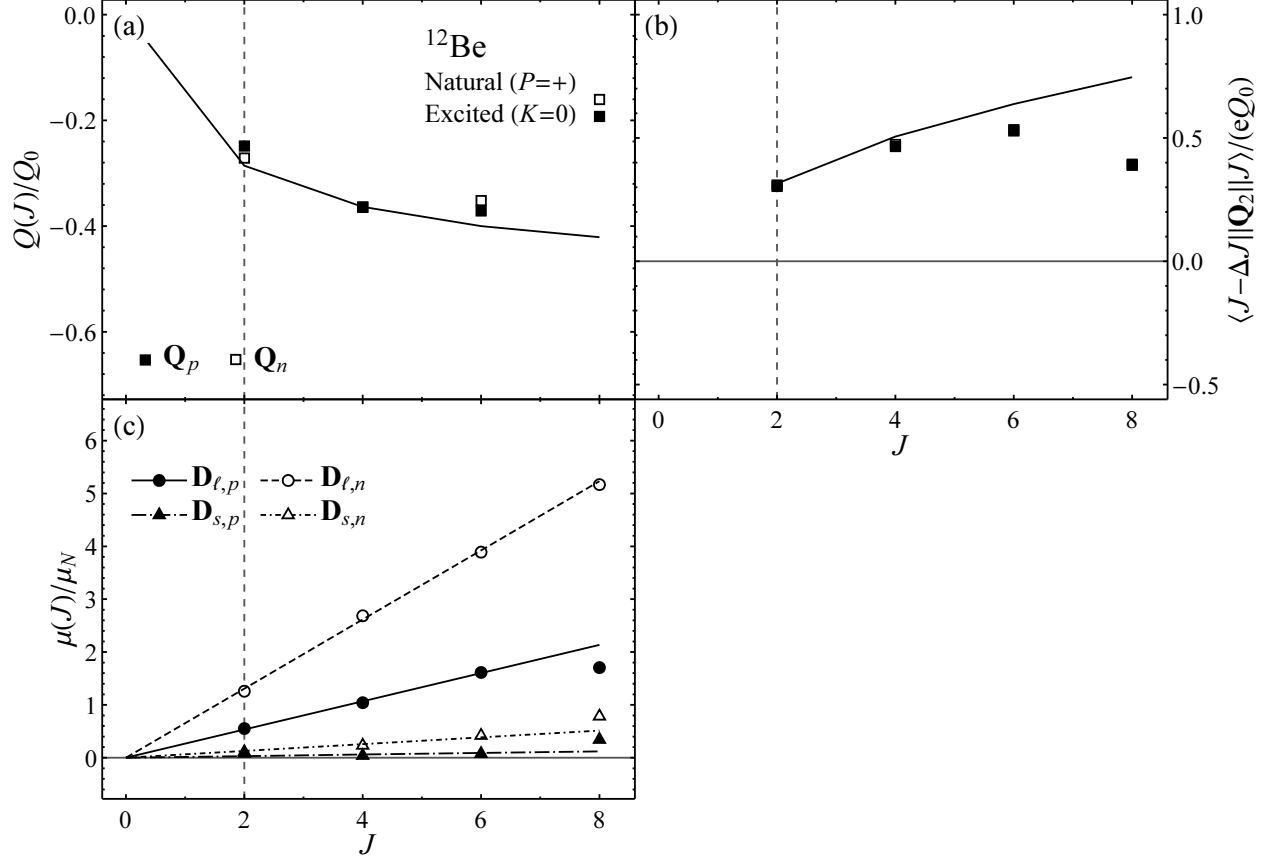


FIG. 15: Dipole and quadrupole matrix element observables for the ^{12}Be natural parity excited band. See Fig. 5 caption for discussion of the plot contents and labeling.

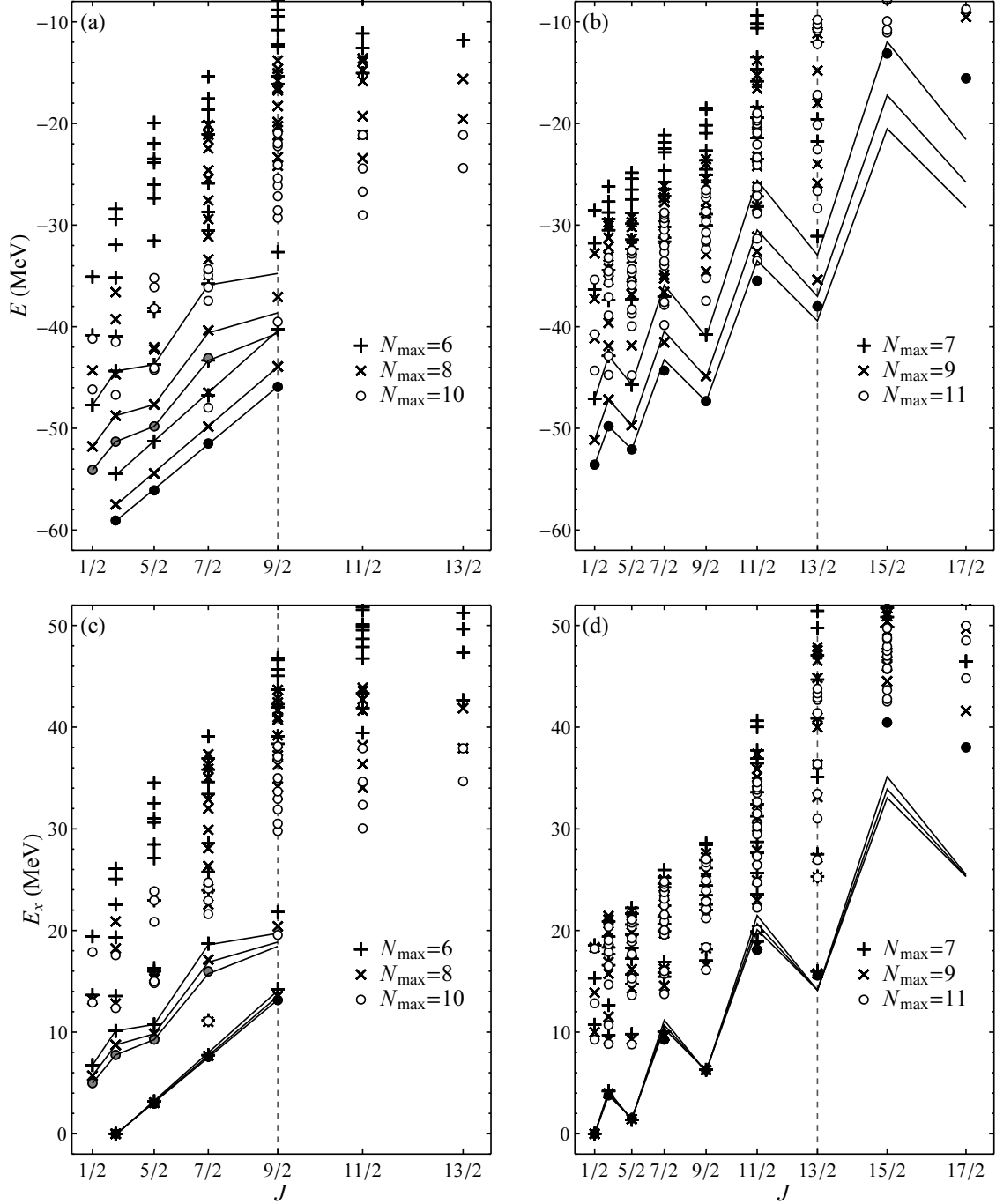


FIG. 16: Dependence of calculated energies for ${}^9\text{Be}$ on the basis truncation N_{max} : absolute energies E (top) and excitation energies E_x (bottom). Low-lying states in the natural (left) and unnatural (right) parity spaces are shown. Calculations are for $6 \leq N_{\text{max}} \leq 10$ for natural parity, or $7 \leq N_{\text{max}} \leq 11$ for unnatural parity (calculations of increasing N_{max} are indicated by plusses, crosses, and diamonds, respectively). Excitation energies are taken separately for each parity. See Fig. 3 caption for discussion of other aspects of the plot contents and labeling.

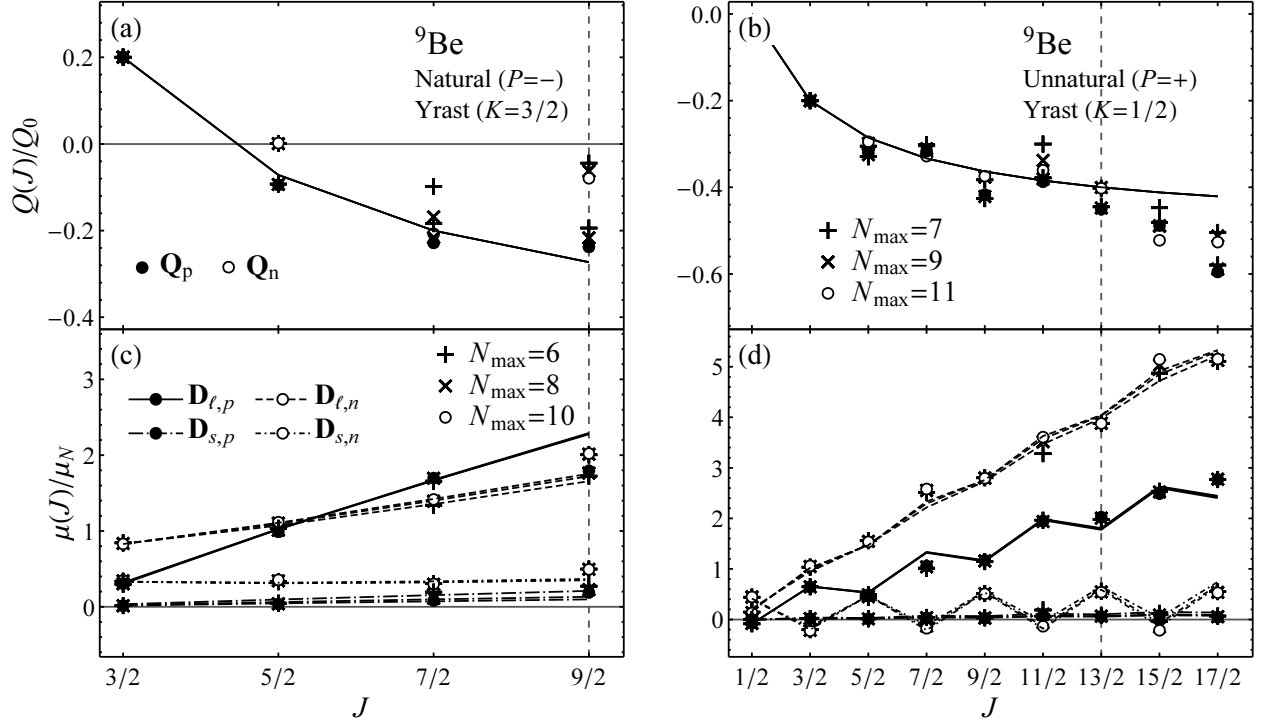


FIG. 17: Dependence of calculated electromagnetic moments for ${}^9\text{Be}$ on the basis truncation N_{max} : quadrupole moments (top) and dipole moments (bottom), of the natural (left) and unnatural (right) parity yrast bands. Calculations are for $6 \leq N_{\text{max}} \leq 10$ for natural parity, or $7 \leq N_{\text{max}} \leq 11$ for unnatural parity (calculations of increasing N_{max} are indicated by plusses, crosses, and circles, respectively). See Fig. 5 caption for discussion of other aspects of the plot contents and labeling.

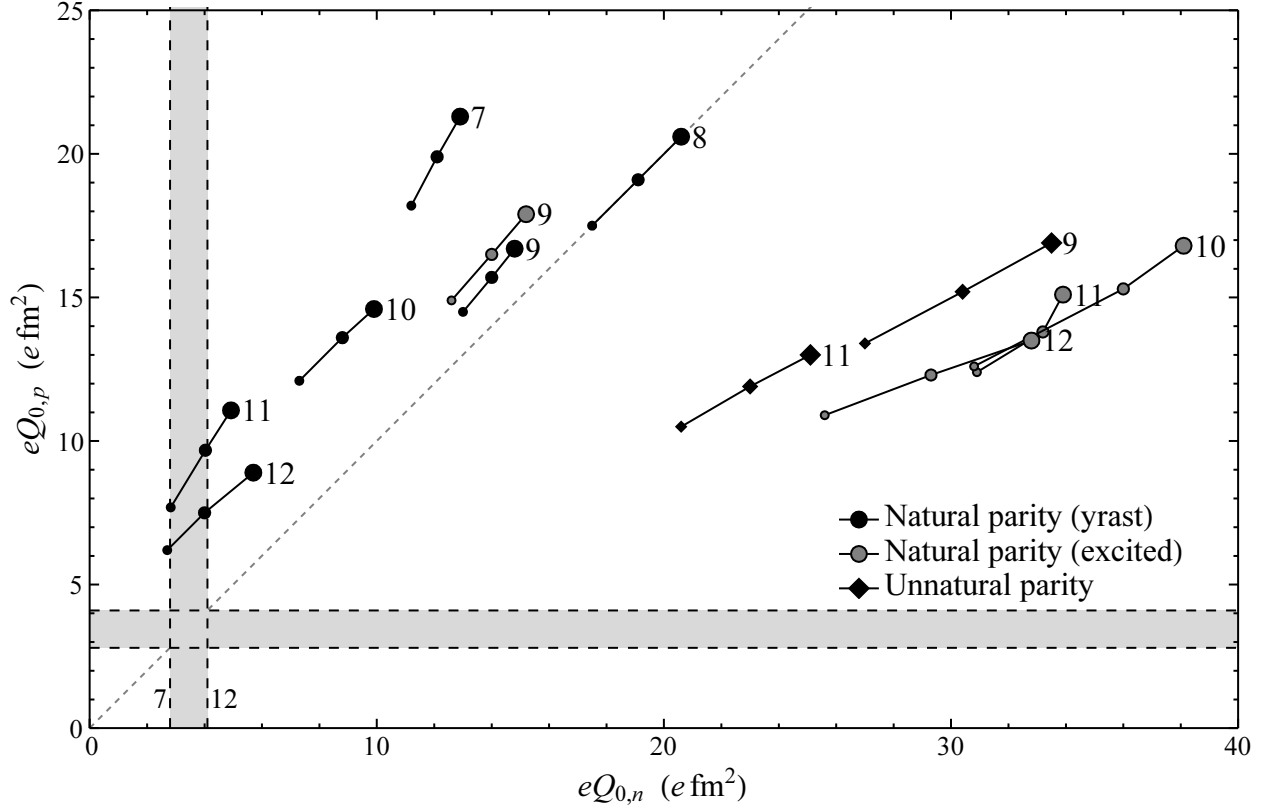


FIG. 18: Intrinsic quadrupole moments plotted as $eQ_{0,p}$ vs. $eQ_{0,n}$, for all bands considered in the present work. Bands are distinguished as natural parity yrast (circles, solid), natural parity excited (circles, shaded), and unnatural parity yrast (diamonds). Data points are labeled by the mass number of the Be isotope. Values are shown for successive N_{\max} values ($6 \leq N_{\max} \leq 10$ for natural parity or $7 \leq N_{\max} \leq 11$ for unnatural parity) to provide an indication of convergence (the larger symbols indicate higher N_{\max} values). The line $Q_{0,p}/Q_{0,n} = 1$ is marked (dashed diagonal line), as is the range of Weisskopf estimates as A ranges from 7 to 12 (shaded bands).

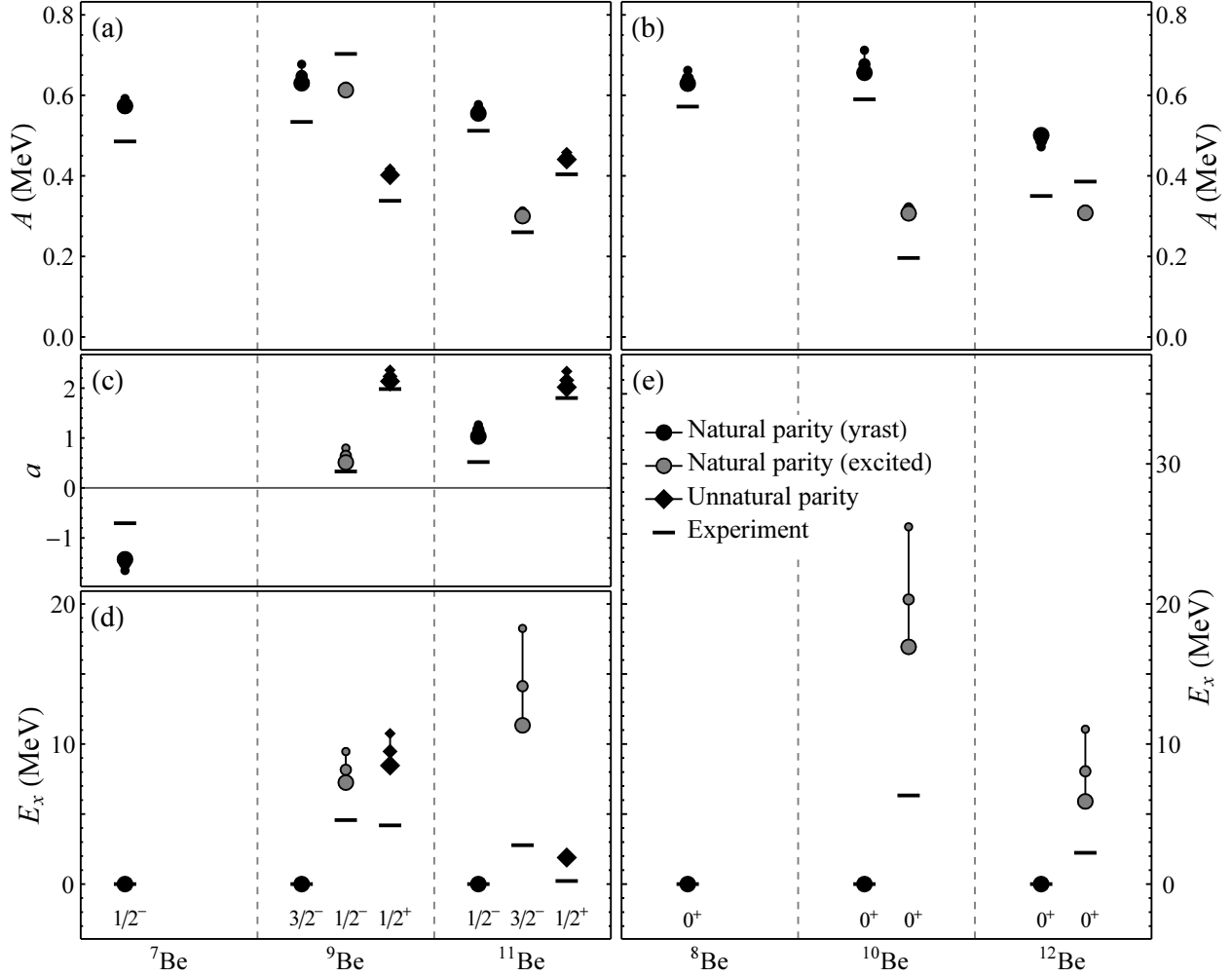


FIG. 19: Band energy parameters for all bands considered in the present work, for the odd-mass Be isotopes (left) and even-mass Be isotopes (right). Parameters considered are: the rotational energy constant A (top), the Coriolis decoupling parameter a (middle), and the band excitation energy E_x (bottom), which is defined as the band energy E_0 for the given band [see (2) and (3)] relative to that of the natural parity yrast band. Bands are distinguished as natural parity yrast (circles, solid), natural parity excited (circles, shaded), and unnatural parity yrast (diamonds). Values are shown for successive N_{max} values (6 $\leq N_{\text{max}} \leq 10$ for natural parity or 7 $\leq N_{\text{max}} \leq 11$ for unnatural parity) to provide an indication of convergence (the larger symbols indicate higher N_{max} values). The parameter values extracted from experimental bands are indicated by horizontal lines. The K^P assignments for the bands are indicated at bottom.

TABLE I: Maximal angular momenta accessible for the Be isotopes in the valence, or $N_{\text{max}} = 0$ space, *i.e.*, lowest oscillator configurations of natural parity. For ${}^9, {}^{11}\text{Be}$, the maximal angular momenta accessible in the $N_{\text{max}} = 1$ space, or lowest oscillator configurations of unnatural parity, are also shown.

Parity	${}^7\text{Be}$	${}^9\text{Be}$	${}^{11}\text{Be}$	${}^8\text{Be}$	${}^{10}\text{Be}$	${}^{12}\text{Be}$
Natural	7/2	9/2	7/2	4	4	2
Unnatural		13/2	13/2			

TABLE II: Magnetic dipole best-fit coefficients for the calculated bands in the odd-mass Be isotopes, as obtained with $N_{\text{max}} = 10$ for natural parity or $N_{\text{max}} = 11$ for unnatural parity, corresponding to the rotational curves in Figs. 5–11. Natural parity bands (upper table) and unnatural parity bands (lower table) are shown separately. Coefficients are in units of μ_N .

	K	$\mathbf{D}_{\ell,p}$			$\mathbf{D}_{\ell,n}$			$\mathbf{D}_{s,p}$			$\mathbf{D}_{s,n}$		
		a_0	a_1	a_2	a_0	a_1	a_2	a_0	a_1	a_2	a_0	a_1	a_2
^7Be	1/2	+0.620	-0.304	+0.460	+0.345	-0.129	+0.143	+0.022	+0.000	+0.013	+0.012	+0.432	-0.615
^9Be	3/2	+0.558	-0.860	—	+0.361	+0.480	—	+0.024	-0.031	—	+0.057	+0.412	—
	1/2	+0.541	-0.281	+0.105	+0.442	+0.656	-0.108	+0.030	+0.003	+0.022	-0.012	-0.377	-0.019
^{11}Be	1/2	+0.702	-0.319	-0.160	+0.162	+0.849	+0.221	+0.079	-0.067	-0.016	+0.057	-0.463	-0.044
	3/2	+0.230	-0.304	—	+0.690	-0.041	—	+0.012	-0.003	—	+0.067	+0.348	—
^9Be	1/2	+0.319	-0.196	-0.380	+0.642	-0.197	-0.175	+0.010	-0.008	-0.013	+0.029	+0.401	+0.569
^{11}Be	1/2	+0.404	-0.124	-0.585	+0.528	-0.243	+0.190	+0.016	-0.003	-0.020	+0.052	+0.370	+0.415

TABLE III: Experimental band members used for the rotational energy fits yielding the experimental rotational parameter values in Fig. 19. For each band member, the nominal J^P (assignments are not all definite, as discussed in the indicated references) and excitation energy (in MeV) are indicated.

Band	Levels	References
${}^7\text{Be } 1/2_1^-$	$1/2^-$ 0.429, $3/2^-$ 0, $7/2^-$ 4.570	[46]
${}^9\text{Be } 3/2_1^-$	$3/2^-$ 0, $5/2^-$ 2.429, $7/2^-$ 6.380	[47, 58]
$1/2_1^-$	$1/2^-$ 2.78, $3/2^-$ 5.59, $5/2^-$ 7.94	[47]
$1/2_1^+$	$1/2^+$ 1.684, $3/2^+$ 4.704, $5/2^+$ 3.049	[47, 58]
${}^{11}\text{Be } 1/2_1^-$	$1/2^-$ 0.320, $3/2^-$ 2.654, $5/2^-$ 3.889	[42, 58, 77]
$3/2_1^-$	$3/2^-$ 3.955, $5/2^-$ 5.255, $7/2^-$ 6.380	[42, 58, 78]
$1/2_1^+$	$1/2^+$ 0, $3/2^+$ 3.400, $5/2^+$ 1.783	[42, 58, 77]
${}^8\text{Be } 0_1^+$	0^+ 0, 2^+ 3.03, 4^+ 11.35	[47, 58]
${}^{10}\text{Be } 0_1^+$	0^+ 0, 2^+ 3.368, 4^+ 11.760	[47, 58, 79]
0_2^+	0^+ 6.179, 2^+ 7.542, 4^+ 10.150	[47, 57, 58, 80]
${}^{12}\text{Be } 0_1^+$	0^+ 0, 2^+ 2.102	[42, 58]
0_2^+	0^+ 2.24, 2^+ 4.560	[42, 58, 64, 66, 81]